Regional validation of the solar irradiance tool SolaRes in clear-sky conditions, with a focus on the aerosol module

Thierry Elias[(1)(*)], Nicolas Ferlay[(2)], Gabriel Chesnoiu[(2)], Isabelle Chiapello[(2)], Mustapha Moulana[(1)]

[(1)] HYGEOS, Euratechnologies, 165 boulevard de Bretagne, 59000 Lille, France

[(2)] Laboratoire d'Optique Atmosphérique, Université Lille, CNRS, UMR 8518, 59000 Lille, France

[(*)] Corresponding author: te@hygeos.com

Abstract

The SolaRes (Solar Resource estimate) tool based on the SMART-G radiative transfer code has the ambition to fulfil both research and industrial applications by providing accurate, precise, and high time resolution simulations of solar resource. We investigate the capacity of SolaRes to reproduce the radiation field, relying on two years of ground-based measurements by pyrheliometers and pyranometers acquired in northern France (Lille and Palaiseau). Our main objective is to provide, as a first step in clear-sky conditions, a thorough regional validation of SolaRes allowing to investigate aerosol impacts. We perform comparisons between SolarRes simulated and clear-sky measured global horizontal irradiance (GHI), direct normal irradiance (DNI), diffuse horizontal irradiance (DifHI), global and diffuse irradiance in tilted plane (GTI, DifTI), and even considering the circumsolar contributions.

Using spectral aerosol optical thickness (AOT) data sets as input, which are delivered by the Aerosol Robotic network (AERONET) and the Copernicus Atmospheric Monitoring Service (CAMS), we examine the influence of aerosol input data sets in SolaRes on the comparison scores. Two aerosol models are mixed to compute aerosol optical properties. We also perform a sensitivity study on the aerosol parametrization, and investigate the influence of applying more or less strict cloud-screening methods to derive te ground-based proof data sets of clear-sky moments.

SolaRes is validated, with the (relative) root mean square difference (RMSD) in *GHI* as low as 1%, and a negligible mean bias difference (MBD). SolaRes also estimates the circumsolar contribution which improves *MBD* in *DNI* and *DifHI*, by 1% and 4% respectively, as well as *RMSD* by ~0.5%. *MBD* in *DNI* is around -1% and *RMSD* around 2%, and *MBD* in *DifHI* is 2% and *RMSD* around 9%. *RMSD* and *MBD* in both *DNI* and *DifHI* are larger than in GHI because they are more sensitive to the aerosol and surface properties. *DifTI* measured in a vertical plane facing South is simulated by SolaRes with an *RMSD* of 8%, comparable to that obtained for clear-sky *DifHI*. Our results suggest a strong influence of reflection by not only ground surface but also surrounding buildings.

The sensitivity studies on the aerosol parameterisation show that the spectral *AOT* contains enough information for high performance in *DNI* simulations, with low influence of the choice of the aerosol models on the *RMSD*. However, complementary information on angular scattering and aerosol absorption provided by the AERONET-inverted model allows to improve simulated clear-sky *GHI* by reducing *RMSD* by ~0.5%, and *MBD* by ~0.8%. Moreover the choice of the data source has a significant influence. Indeed, using CAMS *AOT* instead of AERONET *AOT* increases the *RMSD* in *GHI* by ~1% and *MBD* by ~0.4%, and *RMSD* in *DNI* by 5%. Anyway, *RMSD* in *GHI* still remains slightly smaller than state-of-the-art methods.

footnotes:

(1) https://www-loa.univ-lille1.fr/observations/plateformes.html?p=lille

(2) *https://ads.atmosphere.copernicus.eu/cdsapp#!/dataset/cams-global-atmospheric-composition-forecasts?tab=form*

(3) *https://www.soda-pro.com/web-services/radiation/cams-mcclear*

1. Introduction

Solar radiation incident on collecting systems is one of the main influencing parameters of the electrical productivity by a solar plant. Incident solar radiation is highly variable in time and space because of changing atmospheric optical properties affected by clouds, aerosols, water vapour, ozone, as well as surface reflection and solar direction geometry. The electricity production also depends on the panel orientation and inclination relative to the incident solar radiation direction, and on its spectral absorption efficiency.

The aim of the Solar Resource estimate tool (SolaRes) is to provide precise and accurate simulations of the solar resource at 1-minute resolution for any location on the globe, in any meteorological and ground surface conditions, and for any solar plant technology. SolaRes consequently suits many applications from research to industrial fields. SolaRes is powered by the Speed-up Monte Carlo Atmospheric Radiative Transfer code using GPU (SMART-G) which resolves physically the radiative transfer equation [Ramon *et al.*, 2019]. Until now, physical radiative transfer codes have rarely been used to simulate solar resource for industrial needs in solar energy [e.g. Sun *et al.*, 2019] as they are usually slower than approaches based on abaci or look-up tables. However, the particular design of SMART-G makes it a suitable tool for such endeavours, as computations are hastened through a parallelisation approach on GPU cards. The use of a physical radiative transfer code offers the advantage of precision and accuracy, as well as flexibility.

Moreover, SMART-G could be ranked in the class A (physical radiative transfer code) classification defined by Gueymard and Ruiz-Arias [2015], as any angular and spectral characteristics of the solar radiation field can be computed on demand. This possibility is particularly important for photovoltaic applications as, according to Lindsay *et al.* [2020], computation of spectrally-and-angularly refined irradiances could decrease the error in simulated electrical power produced by photovoltaic set-up (PV) by up to 15%. This is the purpose to use such a code as SMART-G in SolaRes.

SolaRes is firstly described in this paper, which also presents its regional validation. SolaRes, provides not only the global horizontal irradiance (GHI) as the standard solar resource component, but also other components depending on the angular behaviour of the radiation field, as direct normal irradiance (DNI) and the diffuse horizontal irradiance (DifHI), as well as the projected quantities on a tilted plane, i.e. the global tilted irradiance (GTI) and the diffuse tilted irradiance (DifTI). Such components are essential to describe processes involved in solar technologies and also related to vegetation [e.g. Mercado et al., 2009]. Note that SolaRes encompasses the Attenuation of Solar Radiation by Aerosols (ASoRA) method for *DNI* estimates, which has been validated in clear-sky conditions in an arid environment [Elias *et al.*, 2021]. Note that SolaRes also allows computations of the circumsolar contribution, as it provides two estimates of Direct Normal Irradiance (*DNI)*: 1) DNI_{pyr} consistent with observed *DNI*, which include circumsolar contribution; 2) DNI_{strict}, not including circumsolar contribution, but consistent with computations of solar resource parameters in any panel orientation. Usually, physical or semi-physical models provide only one of these two estimates of *DNI*. For example Gueymard and Ruiz-Arias [2015] remind that circumsolar contribution is not considered by any of the 24 models they have selected for their review.

As computation uncertainties come from both the model and the input data set, the validation must be performed with an input data set defined with the best precision. Aerosol optical thickness (AOT) can be measured at local scale with high precision by the ground-based photometers of the Aerosol Robotic NETwork (AERONET) [Holben *et al.*, 1998]. However cloud optical thickness can not be inferred with such a high precision and at the local scale. The regional validation is thus performed in the absence of clouds, i.e. under clear-sky conditions, for which the variability of the solar radiation mainly relates to the influence of aerosols and solar geometry.

A major process thus consists in identifying the clear-sky moments in a region, North of France, characterized by highly variable overcast conditions. Many methods have been defined in the literature. Based on the review of Gueymard *et al.* [2019], we select and adapt two methods presenting contrasted results in terms of representativity of the atmospheric variability which allow us to assess the influence of cloud-screening methods on the evaluation of SolaRes simulations. The first method, based on Garcia *et al.* [2014] accounts for daily *AOT* variability, and is thus quite representative of the site's typical clear-sky atmospheric conditions, while the other cloud-screening method, based on Long and Ackerman [2000], does not account for changes in *AOT*, and thus tends to eliminate clear-sky situations characterized by high aerosol loads.

The field of study of solar energy benefits of other research areas such as the climate studies. Indeed, some of the measurements of solar radiation used here as ground-based proof for validation are acquired by the Baseline Surface Radiation Network (BSRN) [Driemel *et al.*, 2018], which had for first mission to monitor components of the Earth's radiative budget, and their changes with time, with the "*increasing debate on anthropogenic influences on climate processes during the 1980s*" [Driemel *et al.*, 2018]. In the same field, AERONET contributes to the estimate of the global aerosol radiative forcing by validating the aerosol satellite remote sensing retrievals and also aerosol climate models, in the context of the global greenhouse warming. This thus paper presents a radiative closure study. Indeed two categories of independent simultaneously co-located measurements can be related by a radiative transfer code [e.g. Michalsky *et al.*, 2006; Ruiz-Arias *et al.*, 2013]. The regional validation is performed on data sets acquired at Lille and Palaiseau in 2018-2019, both located in northern France.

From a radiation perspective, one of the main impacts of aerosols is to extinguish the direct component of the solar radiation incident at surface level. Spectral AOT consequently efficiently constrains DNI [Elias *et al.*, 2019; Elias *et al.*, 2021]. Spectral AOT also partly describes the aerosol scattering properties which significantly affect *DifHI*. However some information is missing on aerosol absorption, and surface reflection. Sensitivity studies are then performed to show the efficiency and the limits of the SolaRes tool.

Section 2 describes the observational and modelling data sets used as input of SolaRes, as well as the solar irradiance measurements used as ground-based proof for validation. ***Section 3*** briefly describes SMART-G, and the parameterisations used in SolaRes, especially that related to the aerosol optical properties. ***Section 4*** presents two cloud-screening procedures, and investigates their impact on the validation data set, and on the factors affecting radiative transfer such as AOT. ***Section 5*** presents the results of the comparison performed between SolaRes estimates and solar irradiance ground-based measurements. Eventually, ***Sect. 6*** shows the sensitivity of the comparison scores to the aerosol parameterisation, considering two main influences: 1) the hypothesis on mean aerosol nature, 2) the aerosol data source. Indeed the Copernicus Atmospheric Monitoring Service (CAMS), assimilating satellite data sets to describe air quality on a global scale, is also used here as an input data provider.

2. Data

Our analysis of SolaRes performances relies on different types of data. SolaRes requires input data provided either by a ground-based instrumentation network (***Sect. 2.3***), or by a global atmospheric model (***Sect. 2.4***). The solar resource components simulated by SolaRes (***Sect. 3***) are validated (***Sect. 5***) by comparisons with ground-based measurements (***Sect. 2.2***)

2.1. Choice of the two sites

Two platforms located in northern part of France are chosen, both embedded in sub-urban environment, and both hosting a comprehensive set of radiative instruments. This choice is motivated by several arguments.

First, downwelling solar irradiance is measured at surface level with a distinction of direct and diffuse components, at both sites. Measurements of Palaiseau (France, 48.7116°N, 2.215°E, 156 m a.s.l.) contribute to the Baseline Surface Radiation Network (BSRN) [Driemel *et al.*, 2018], which brings a high source of confidence. Measurements on the ATOLL (ATmospheric Observations in LiLLe) platform (France, 50.61167°N, 3.141670°E, 60 m a.s.l.) are also of quality, well confidently known by the authors (one of them being the PI of the instruments), and the site provides in addition interesting solar irradiance measurements in tilted planes that are exploited in the subsection 5.4.

Secondly, the two sites provide accurate measurements of aerosol loading as they are AERONET sites. Third, the aerosol loading above these two sites is quite representative of observations over western Europe. While not at the level of high loading due to natural aerosol (e.g. desert dust) or strong anthropogenic emissions (e.g. some areas in China or India), the observed aerosol loading is moderate for European standards. The aerosol loadings are quite variable and diverse, resulting from changing meteorology, as with oceanic relatively clean influence in the case of west wind often occurring in winter, versus continental influence during anticyclonic situations often occurring in spring. The continental influence transports anthropogenic pollution from road traffic and agriculture. According to the Köppen–Geiger climate classification [Beck *et al.*, 2018], both sites are affected by a climate similar to western Germany [Witthuhn et al., 2021], and to England, Ireland, Belgium, Netherlands, which is labelled Cfb.

The last arguments to retain these sites is that cloudy situations are numerous. So these two sites are appropriate to test cloud-screening techniques, particularly those that won't falsely reject clear-sky conditions with loader than pristine conditions.

2.2. Ground-based irradiance measurements used as a validation data set

2.2.1. The ATOLL platform

Since 2008, a set of class A Kipp&Zonen instruments mounted on an EKO sun tracker (STR-22) measures routinely the solar downward irradiance on the ATOLL (ATmospheric Observations in LiLLe) platform (France, 50.61167°N, 3.141670°E, 60 m a.s.l.), at the campus of Lille University(footnote 1) (the site is named 'Lille' in the paper). A CHP1 pyrheliometer (Kipp & Zonen, 2008) measures the direct normal irradiance (DNI_{obs}), in a field of view of 5±0.2°. A CMP22 pyranometer (Kipp & Zonen, 2013) associated with a shadowing ball measures the diffuse horizontal irradiance ($DifHI_{obs}$). Both DNI_{obs} and $DifHI_{obs}$ are provided at 1-minute resolution.

Calibrations performed in 2012, 2017 and 2022 show a relative stability of the instrument performances. Indeed the CHP1 calibration coefficient varies by a maximum of 3% over the period, and the CMP22 calibration coefficient decreases by less than 1%. According to Witthuhn *et al.* [2021], the uncertainty under clear-sky conditions is 2% for *GHI* and larger for *DifHI (4%)* because of the shadowing device, and is 5% for *DNI*. Winter gaps of a few weeks exist in the data time series when the instruments are sent either in Delft (Netherlands) for a recalibration (by Kipp and Zonen) or in M'Bour (Senegal) to be used as references for calibration of local instruments.

Observed global horizontal irradiance (GHI_{obs}) at Lille is obtained as the sum of direct and diffuse components, which is the preferred method for the measurement of global irradiance [Flowers and Maxwell, 1986], avoiding most cosine response's error of the instrument at low sun angles [Michalsky and Harrison, 1995; Mol *et al.*, 2024], and affected by smaller uncertainties in GHI_{obs} than with unshaded instruments [Michalsky *et al.*, 1999]. The summation is indeed chosen by BSRN [Ohmura *et al.*, 1998], and can be expressed as:

$$GHI_{obs} = DirHI_{obs} + DifHI_{obs}, \quad (1a)$$

$$\text{with } DirHI_{obs} = DNI_{obs}\ \mu_0 \quad (1b)$$

where $\mu_0 = \cos(SZA)$, and *SZA* is the solar zenith angle.

Additionally, since 2017, the ATOLL platform also hosts an unshaded class A Kipp&Zonen CMP11 pyranometer which measures the global tilted irradiance (GTI_{obs}) for various inclinations. Both the CHP1 and CMP22 instruments measure radiation in the broadband range between 210 and 3600 nm, while the spectral range for the CMP11 pyranometer extends between 270 and 3000 nm.

Note that the CMP11 is set horizontally in spring-summer 2018 for an intercomparison campaign with both CHP1 and CMP22. Comparison is made during clear-sky minutes found over 47 days (according to the Garcia cloud-screening method presented in ***Sect. 4***). The mean relative difference between GHI_{obs} measured by the CMP11 and by the CHP1+CMP22 instruments is found to be -8±5 W/m^2 (1.6±0.9%) (CMP11 providing smaller values than CHP1+CMP22), and the root mean square difference (RMSD) is 9 W/m^2 (1.9%), within the instrumental uncertainties.

Our analysis focuses on the 2018-2019 time period which is close to the 2017 calibration, and includes the intercomparison campaign of 2018, as well as the time period with vertical CMP11 in 2019, which allows validation of SolaRes under different angular configurations.

2.2.2. BSRN site of Palaiseau

Solar resource measurements are made at Palaiseau (France, 48.7116°N, 2.215°E) as part of BSRN, by three Kipp&Zonen CHP1 and CMP22 instruments, similar to those running in Lille. GHI_{obs} and DNI_{obs} are measured by CMP22 and CHP1, respectively, and $DifHI_{obs}$ is measured by a second CMP22 mounted with a sun-tracking shadower device. A 1-Hz sampling rate is recommended for radiation monitoring, and measurements are recorded and provided at 1-minute time resolution. Uncertainty requirements for the 1-minute BSRN data are 5 W/m^2 for $DifHI_{obs}$, and 2 W/m^2 for DNI_{obs} [Ohmura *et al.*, 1998].

2.3. AERONET providing input data sets on aerosols and water vapour

Coincidentally to the irradiance measurements, AERONET photometers [Holben *et al.*, 1998] acquire measurements at both Lille and Palaiseau. We use direct measurements of aerosol optical thickness (AOT) at both 440 and 870 nm, as well as the column water vapour content (WVC) as input to the SolaRes algorithm. We use the Level 2.0 data quality, applying a clear-sun cloud-screening, and the V3 version of AERONET data [Sinyuk *et al.*, 2020], which also provides ozone content from "*Total Ozone Mapping Spectrometer (TOMS) monthly average climatology (1978–2004)*". The expected uncertainty in *AOT* is 0.01-0.02 at these wavelengths [Dubovik *et al.*, 2000; Giles *et al.*, 2019]. *AOT* measurements are made at the sampling rate of around 3 minutes [Giles *et al.*, 2019], in clear-sun conditions. .

In addition to AOT measurements at several wavelengths, AERONET provides inverted aerosol models at around 1 hour resolution, which are composed of the phase function and the aerosol single scattering albedo at several wavelengths. Level 2.0 inverted data set being too sparse, it limits the statistical significance of our assessment, we then choose to use the Level 1.5 inversion data as other authors [Ruiz-Arias et al., 2013; Cheng et al., 2021; Witthuhn et al., 2021], despite probable larger uncertainties. A Indeed Ruiz-Arias *et al.* [2013] mention an increase in uncertainty of Level 1.5 (V2) aerosol single scattering albedo (*SSA)* compared to Level 2.0, to the 0.05–0.07 range, while Witthuhn et al. [2021] mention an uncertainty of 0.03 for Level 1.5, consistently with an uncertainty of ±0.03 on the V3 Level 2 by Sinyuk *et al.* [2020]. The option "hybrid scan" [Sinyuk *et al.*, 2020] is chosen.

absorption. AOT at 3-minute is chosen to generate the SolaRes input data for validation (Section 5), the 1-hour AERONET-inverted aerosol models are used for a sensitivity study (Section 6.2).

2.4. CAMS providing input data sets on aerosols, water vapour, and surface albedo

Data from the Copernicus Atmosphere Monitoring System (CAMS) [Benedetti *et al.*, 2009; Morcrette *et al.*, 2009] are used to investigate the sensitivity of SolaRes to the aerosol data source (***Sect. 6.3***). To be consistent with an operational near real time (NRT) service, the CAMS-NRT data set is used. *AOT* is provided by CAMS-NRT at several wavelengths, as well as WVC and ozone content. The spatial resolution is 0.4°, and the time resolution is 1 hour. For the paper, global CAMS-NRT data sets are downloaded from the Atmosphere data Store(footnote 2). CAMS-NRT *AOT* at 469 and 865 nm are used to compute the Ångström exponent α (indicator of the spectral dependence of AOT), that allows to infer *AOT* at both 440 and 870 nm (see for example Witthuhn *et al.* [2021]), used as input by the SolaRes algorithm (see ***Sect. 3.3.2***). The Ångström exponent is expressed as:

$$\alpha = \ln\left(\frac{AOT(\lambda_1)}{AOT(\lambda_2)}\right) \Big/ \ln\left(\frac{\lambda_1}{\lambda_2}\right) \quad (2)$$

The comparison with AERONET direct measurements gives an *RMSD* of ~50% in *AOT* (0.10 at 440 nm, and 0.04 at 870 nm), and of 25% (0.3) for α . The *MBD* is smaller than 5% in both *AOT* and α . These comparison results are similar to that of Witthuhn *et al.* [2021] and references therein, over Germany for the CAMS reanalysis data set.

CAMS-NRT data time series at Lille and Palaiseau are also downloaded from the CAMS-radiation service(footnote 3). The 'research mode' allows to download not only *GHI*, *DNI*, and *DifHI*, but also the input data for the model, such as the solar broadband surface albedo, which is derived from the Moderate Resolution Imaging Spectroradiometer (MODIS) as described by Lefèvre *et al.* [2013]. It is a combination of the white-sky and black-sky albedos, in function of the proportion of the direct radiation in the global radiation [Lefèvre *et al.*, 2013]. Daily averages are computed, varying between 0.12 in November-December and 0.16 in June-July at Lille and Palaiseau, and are used as input in SolaRes radiative transfer simulations. Constant value is used by Lindsay et al. [2020], which is slightly larger than values used here for Palaiseau: "*broadband surface albedo [...] set to 0.2, a typical broadband value for grassland*".

3. The SolaRes algorithm

Computations are made with the SolaRes V1.5.0 algorithm. SolaRes computes *DNI* according to the ASoRA method [Elias *et al.*, 2021], and the diffuse irradiance with the SMART-G code [Ramon *et al.*, 2019]. The advantage in using SMART-G is to compute precisely the angular behaviour of the diffuse radiation field, by considering aerosol and surface optical properties: *DifHI* can be computed as well as *DifTI* for any inclination and orientation, and the circumsolar contribution can be estimated by computing the diffuse irradiance in a narrow field of view centred on the solar direction.

To better reproduce the solar resource time variability, and to better evaluate the performances of SolaRes in clear-sky conditions, computations are made at a 1-minute time resolution, as advised by several authors such as Sun *et al.* [2019]. On the one hand, *DNI* is computed at the time resolution of 1 minute by interpolating aerosol optical thickness at 1 minute. On the other hand, *DifHI* is computed at 15-minute resolution by radiative transfer computations with SMART-G, to limit the computational time, and is then interpolated linearly at the 1-minute resolution. *GHI* is computed by adding 1-minute *DNI* projected on the horizontal plane (*DirHI*) and 1-minute *DifHI*, as done by all high-performance models referenced by Sun *et al.* [2019], and a similarly method is used for *GTI*:

$$\mathrm{GHI} = \mathrm{DirHI} + \mathrm{DifHI} \tag{3a}$$

$$\mathrm{GTI} = \mathrm{DirTI} + \mathrm{DifTI} \tag{3b}$$

3.1. The direct contribution

3.1.1. DNI_{strict}, and its projection

While *DifHI* and *DifTI* are computed with SMART-G (***Sect. 3.2***), *DirHI* and *DirTI* are computed by projecting *DNI* on a horizontal or tilted plane:

$$\mathrm{DirTI} = \mathrm{DNI} \quad \overrightarrow{\Omega_S} \cdot \vec{n} \tag{4}$$

with $\overrightarrow{\Omega_S}$ the unit vector in the solar direction:

$$\overrightarrow{\Omega_S} = \left(\sin(SZA)\cos(SAA)\,;\sin(SZA)\sin(SAA)\,;\cos SZA\right) \quad , \tag{5}$$

where *SAA* is the solar azimuthal angle, and $\vec{n}$ is the unit vector perpendicular to the titled surface:

$$\vec{n} = \left(\sin i \cos o\,;\sin i \sin o\,;\cos i\right) \quad , \tag{6}$$

where *i* is the inclination of the titled surface and *o* its orientation, relative to the North and increasing eastward (as SAA). If the plane is horizontal, i=0, $\overrightarrow{\Omega_S} \cdot \vec{n} = \cos(SZA)$, we get DirHI = DNI μ_0 (***Eq. (1b)***).

DNI can either be DNI_{strict} according to the 'strict' definition given by Blanc *et al.* [2014], or DNI_{pyr} as it is observed by a pyrheliometer. For DNI_{strict}, only beams in the solar direction are counted, which are not scattered by the atmosphere. In other words, the circumsolar radiation is not accounted for. Underestimation of DNI_{obs} by the DNI_{strict} method is thus expected. Consistently with the ASoRA method [Elias *et al.*, 2021], DNI_{strict} is expressed as:

$$DNI_{strict} = F_{ESD} \int_{\lambda_{inf}}^{\lambda_{sup}} E_{sun}(SZA, \lambda) T_{col}(SZA, \lambda) d\lambda \quad . \tag{7}$$

F_{ESD} is the Earth-Sun distance correcting factor. The spectral integration is made between the two wavelengths λ_{inf} and λ_{sup}. $E_{Sun}(\lambda)$ corresponds to the extra-terrestrial solar irradiance at the wavelength λ. $T_{col}(SZA, \lambda)$ represents the atmospheric column transmittance, which can be decomposed, under clear-sky conditions, as:

$$T_{col}(\lambda) = T_{Ray}(\lambda) \, . \, T_{gas}(\lambda) \, . \, T_{aer}(\lambda), \tag{8}$$

where *SZA* is omitted for clarity. $T_{Ray}(\lambda)$ is the transmittance caused by Rayleigh scattering, along the atmospheric column, while $T_{gas}(\lambda)$ is caused by absorbing gases, mainly water vapour and ozone in the solar spectrum. In clear-sky conditions, $T_{col}(\lambda)$ does not depend on the cloud transmittance. $T_{aer}(\lambda)$ is defined according to the Beer-Lambert-Bouguer law as:

$$T_{aer}(\lambda) = e^{-m_{air} AOT(\lambda)} \quad . \tag{9}$$

where m_{air} is the optical air mass which can be approximated by $1/\mu_0$, and must take into account the Earth's sphericity for *SZA* above 80° [e.g. Kasten and Young, 1989].

3.1.2. Considering the circumsolar contribution

The pyrheliometer measures not only beams in the solar direction but also all scattered radiation within the instrument field of view. The difference between observation and simulation is then expected to decrease by considering DNI_{pyr} defined as:

$$DNI_{pyr} = DNI_{strict} + \Delta DifNI_{circ}, \tag{10}$$

where $\Delta DifNI_{circ}$ is the circumsolar contribution on a plane perpendicular to the solar direction. Moreover, the sun-tracking shadowing device, which allows a pyranometer to measure *DifHI* instead of *GHI*, does not block only direct radiation but also radiation scattered around the sun. $DifHI_{pyr}$ is then defined as:

$$DifHI_{pyr} = DifHI_{strict} - \Delta DifHI_{circ}, \quad (11)$$

with

$$\Delta DifHI_{circ} = \Delta DifNI_{circ}\ \mu_0 \quad (12)$$

3.2. Brief description of SMART-G

SMART-G allows to simulate the propagation of polarised light (monochromatic or spectrally integrated), in a coupled atmosphere-ocean system in a plane-parallel or spherical-shell geometry, as described by Ramon *et al.* [2019]. The code uses General-Purpose Computation on Graphic Processing Units technology with other Monte Carlo variance reduction methods (local estimation [Marchuk *et al.*, 1981], ALIS [Emde *et al.*, 2011], etc.) to speed up the simulations while keeping high precision.

In this work SMART-G is used to simulate all diffuse irradiance parameters i.e. *DifHI*, *DifTI*, and $\Delta DifNI_{circ}$, in a plane-parallel atmosphere. *DifHI* is calculated by using the simple conventional method for planar flux in Monte Carlo radiative transfer codes, where the solar rays are tracked from the sun to the ground. The scattered rays reaching the ground surface are then counted to calculate *DifHI*. For *DifTI* we use a backward Monte Carlo tracking of solar radiation i.e. the solar radiation rays are followed in the inverse path, from the instrument to the sun, with the local estimation method [Marchuk *et al.*, 1981] to reduce the variance. The half aperture angle is 90° to imitate the pyranometer. The circumsolar contribution $\Delta DifNI_{circ}$ is calculated similarly to *DifTI* but by assigning a half aperture angle of 2.5° to imitate the pyrheliometer.

3.3. The radiative transfer parameterisation

3.3.1. Atmospheric gases and the surface

The extra-terrestrial solar spectrum is taken from Kurucz [1992]. Rayleigh optical thickness is computed according to Bodhaine *et al.* [1999], and scaled with the atmospheric pressure. The gas and thermodynamic profiles are adopted from the AFGL US summer standard atmosphere [Anderson *et al.*, 1986], providing the water vapour optical thickness, which is scaled linearly with WVC from the input data source. Ozone and NO_2 absorption cross sections are taken from Bogumil *et al.* [2003], and we use the absorption band parameterisation provided by Kato *et al.* [1999] for other gases like H_2O, CO_2, CH_4. As UV-C radiation below 280 nm is absorbed by the atmosphere, spectral integration is made between 280 and 4000 nm for comparisons with CHP1 and CMP22 measurements, and between 280 and 3000 nm for comparisons with CMP11 measurements. In k-distribution parametrization, the bands between 280 and 4000 nm corresponds to 30 spectral intervals with 297 Gaussian quadrature points named g-points [Lacis and Oinas, 1991; Kato *et al.*, 1999], and the bands between 280 and 3000 nm corresponds to 28 spectral intervals with 267 g-points. Surface is considered Lambertian, with a spectrally independent albedo.

3.3.2. Aerosol parameterisation

The measurements only partially describe the necessary input aerosol optical properties for radiative transfer computations. It is therefore compulsory to employ various strategies to get the necessary parameters from observation data sets. In SolaRes similarly to the ASoRA method [Elias *et al.*,

2021], it is chosen to mix two aerosol models AM1 and AM2 which reproduce input *AOT* at two wavelengths, such as:

$$AOT_{input}(\lambda_1) = w_{AM1}\, AOT_{AM1}(\lambda_1) + w_{AM2}\, AOT_{AM2}(\lambda_1) \quad (13a)$$

$$AOT_{input}(\lambda_2) = w_{AM1}\, AOT_{AM1}(\lambda_2) + w_{AM2}\, AOT_{AM2}(\lambda_2) \quad (13b)$$

where $AOT_{input}(\lambda)$ is provided by AERONET or CAMS-NRT, and $AOT_{AM1}(\lambda)$ and $AOT_{AM2}(\lambda)$ are computed here from two aerosol models from the Optical Properties of Aerosols and Clouds (OPAC) database [Hess *et al.*, 1998]. To span a large range of Ångström exponent (α) values, it is recommended that one model is characterised by a large value of α and another by a smaller value of α. We then refer to a small-α model and to a large-α model. λ_1 and λ_2 are 440 and 870 nm, respectively. The weights w_{AM1} and w_{AM2} are obtained from ***Eq. (13a) and (13b)***, and are used to compute the aerosol transmittance at other wavelengths of the 280-4000 nm spectral interval. For the computation of the diffuse radiation components by SMART-G, the weights w_{AM1} and w_{AM2} are also applied to the aerosol phase function and single scattering albedo. 3-minute *AOT* is chosen to generate the SolaRes input data, because:

1) The main factor on *GHI* and *DNI* is *AOT*, which is proportional to the aerosol burden in the atmospheric column

2) *AOT* is the usual aerosol information provided in both observation and modelling data sets.

3) *AOT* is often provided at several wavelengths of the solar spectrum. Spectral *AOT*, or the Ångström exponent, is indicative of the aerosol size, and consequently party informs about the aerosol nature.

4) the 3-minute resolution is adapted to follow any time evolution in aerosol burden and nature.To reduce the computational burden and the number of radiative transfer computations, the AERONET data set is averaged at 15-minute and aerosol optical properties are generated at the resolution of 15-minute to compute *DifHI*. 15-min *AOT* is then interpolated at 1-minute to compute 1-min *DNI*.

For the sensitivity study of ***Sect. 6.2***, the AERONET inverted aerosol model provides the aerosol phase function and single scattering albedo at the four wavelengths of 440, 675, 870 and 1020 nm [Sinyuk et al., 2020]. In this case, *AOT* and the aerosol single scattering albedo (SSA) are linearly interpolated between 440 and 1020 nm, *AOT* is linearly extrapolated below 440 nm and above 1020 nm while SSA remains constant, and the phase function at the closest wavelength is used. The vertical profile of *AOT* decreases exponentially with a vertical height of 2 km.

4. Application of cloud-screening methods based on measured irradiances

The validation is performed in clear-sky conditions, when aerosols directly affect the surface solar irradiance but not the clouds. This section describes two cloud-screening methods, relying on time series of solar irradiance measurements, selected based on the work of Gueymard *et al.* [2019] who compare the outputs of several cloud-screening algorithms, to cloud cover observations by ground-based sky imagers, for several locations in the United States of America. The two methods are expected to show contrasted results in terms of comparison scores, as detailed in ***Sect. 5***.

4.1. Choice of the cloud-screening procedure

Since the output of cloud-screening methods is binary, e.g. the sky is either cloudy or clear, Gueymard *et al.* [2019] evaluate the performances of the cloud-screening methods with a confusion matrix. As the aim of our study is to validate SolaRes simulations in clear-sky conditions, we need to select a cloud-screening method that maximizes the number of correctly identified clear-sky cases, or the True Positive score (TPS). It is also important to keep the False Positive score (FPS) as low as possible to avoid cases of incorrect identification and to minimise cloud contamination. The precision score PS may represent the performance of the screening method in identifying clear-sky moments:

$$PS = \frac{TPS}{TPS+FPS} \tag{14}$$

Based on the TPS and FPS scores presented in Gueymard *et al.* [2019], the cloud-screening algorithm of Garcia *et al.* [2014] (thereafter named Garcia) is retained as it shows the highest PS of 24.0%, and a relatively low FPS of 8.4% [Gueymard *et al.*, 2019]. In addition, the algorithm of Long and Ackerman [2000] (thereafter named L&A) is retained as it shows the lowest FPS of 7.2 %, with PS of 20.8% [Gueymard *et al.*, 2019], as an alternative with fewer misidentified clear-sky moments.

4.2. Description of the chosen cloud-screening procedure

Both Garcia and L&A cloud-screening methods rely on the same series of four tests based on GHI_{obs} and $DifHI_{obs}$ measurements. However Garcia method relies on collocated *AOT* information in order to distinguish between the presence of clouds and the clear-sky situations with higher aerosol loads.

The first two tests remove obvious cloudy minutes characterized by extreme values of the normalized global irradiance GHI_N (test 1) and $DifHI_{obs}$ (test 2) through the definition of threshold values. The third and fourth tests can detect more subtle cloud covers by analysing the temporal variability of GHI_{obs} (test 3) and of the normalised diffuse irradiance ratio $D_{R,N}$ defined as the normalised value of the diffuse ratio $D_{R,obs}$, which is $DifHI_{obs}$ divided by GHI_{obs} (test 4). Note that the goal of the normalization step in the first and fourth tests is to lessen the dependency of GHI_{obs} and $DifHI_{obs}$ with respect to *SZA*. The use of such normalized quantities tends to eliminate early morning and late evening events indiscriminately of the cloud cover [Long and Ackerman, 2000]. This behaviour has limited impact in this study as the data set is selected with *SZA* smaller than 80°.

The four tests are applied in an iterative process to provide each time a new collection of clear-sky moments on which to fit at a diurnal scale, and a set of daily coefficients $a_{GHI/DR,day}$ and $b_{GHI/DR,day}$:

$$GHI_{obs} = a_{GHI,day}\,\mu_0^{b_{GHI,day}} \tag{15a}$$

$$D_{R,obs} = a_{D_R,day}\,\mu_0^{b_{D_R,day}} \tag{15b}$$

where the two coefficients $a_{GHI,day}$ and $a_{DR,day}$ represent the associated clear-sky GHI and $D_{R,obs}$ for SZA=0°, respectively, and the two coefficients b_{GHI} and $b_{DR,day}$ represent their variations with μ_0 for each day. The daily values of each coefficient are then averaged over the available collection of clear-sky days to determine the new annual coefficients $a_{GHI/DR}$ and $b_{GHI/DR}$ over the database, which are then used for the normalization of the measurements in the first and fourth tests. A new set of

$a_{GHI/DR}$ and $b_{GHI/DR}$ parameters is determined for each iteration, until convergence is reached within 5%. This method is thus quite versatile and can be applied to any site equipped with measurements of both *GHI* and *DifHI*.

Table 1 compares the initial values of the coefficients from Long and Ackerman [2000] and Garcia *et al.* [2014] with the ones found for our study conducted in Lille and Palaiseau over the period 2010-2020. The parameters $GHI_{N,min}$ and $GHI_{N,max}$ correspond to the normalized global irradiance thresholds used in the first test to constrain GHI_N. These thresholds are computed as $\mathrm{GHI}_{\mathrm{N,}\,\frac{\max}{\min}} = \mathrm{a_{GHI}} \pm 100\,\mathrm{W.m^{-2}}$. The application of the initial L&A method in Lille and Palaiseau produces equivalent scalable parameters $GHI_{N,min,}$ $GHI_{N,max}$, b_{GHI} and b_{DR} for both sites.

Garcia *et al.* [2014] modify the L&A method to make it applicable to the particular conditions of the Izana Observatory in the Canary Islands, a high-elevation arid site. They show that the daily mean coefficients $a_{GHI,day}$ and $b_{GHI,day}$ found for that site were somewhat correlated to the variations of *AOT* measured coincidentally at 500 nm. Note that as aerosol loadings are quite different between Canary Islands and Northern France, a parametrization more representative of the specific conditions of Lille and Palaiseau was defined in this study. The variation of $a_{GHI,day}$ with respect to *AOT* in Lille and Palaiseau was found to be similar to the one used in Garcia *et al.* [2014]. However, the correlation coefficient is only 0.20, which is lower than the value reported by Garcia *et al.* [2014]. Additionally, the correlation coefficient for b_{GHI} is only 0.30, which is significantly smaller than the value of Garcia *et al.* [2014].

In the present study, the variability of the coefficient b_{DR} relatively to *AOT* is also investigated using various parameterisations. The highest correlation coefficient of 0.31 is found when using a power law of *AOT*. Since this correlation coefficient is close to the one found for b_{GHI}, we slightly modify the Garcia method by including the change of b_{DR} with respect to *AOT* (***Table 1***).

Table 1. Main parameters used by the cloud-screening methods of Long and Ackerman [2000] (L&A) and Garcia *et al.* [2014] (Garcia). It includes the values initially reported in the literature as well as those found specifically for Lille and Palaiseau for the period 2010-2020. *AOT* is the aerosol optical thickness measured at 500 nm.

Test number	Parameter	Cloud-screening method and source				
		L&A			Garcia	
		Literature	Lille	Palaiseau	Literature	Lille and Palaiseau
1st test	a_{GHI} (W/m^2)	/	1153	1140	$1054 \cdot AOT^{-0.03}$	
	$GHI_{N.min}$ (W/m^2)	1000	1053	1040	$1054 \cdot AOT^{-0.03} - 100$	
	$GHI_{N.max}$(W/m^2)	1250	1253	1240	$1054 \cdot AOT^{-0.03} + 100$	
	b_{GHI}	1.20	1.23	1.21	$0.41 \cdot AOT + 1.09$	$0.17 \cdot AOT + 1.21$
4th test	b_{DR}	-0.80	-0.67		-0.62	$-0.54 \cdot AOT^{-0.09}$

4.3. Impact of the cloud-screening procedures

Table 2 shows averaged values of the observed solar resource parameters in 2018-2019, under both all-sky and clear-sky conditions, and for both cloud screening methods. In addition ***Table 3*** shows

averaged values of the key atmospheric properties observed by AERONET, that are most relevant for radiative transfer simulations of the solar resource components under clear-sky conditions, and ***Fig. 1*** shows the seasonal dependence of *AOT* and *WVC*. Note that for Table 3, we use AERONET Level 2.0 data, which is automatically cloud-screened in the only solar direction (i.e. clear-sun). When coincident photometric and irradiance measurements are available, we are able to select AERONET measurements coincident with cloud-free irradiance data points identified by either two irradiance cloud-screening methods (clear-sun & sky). In what follows, *SZA* is constrained below 80°. Winter is composed by December-February, spring by March-May, summer by June-August and autumn by September-November.

Overall, 14 to 16% of observed situations are identified as clear-sky by the Garcia algorithm in 2018-2019 at Lille and Palaiseau, while clear skies only represent 8 to 10% of observations according to the stricter L&A cloud-screening method (***Table 2***). The proportion of clear-sky moments in summer is more than twice larger than in winter according to Garcia, and larger by ~35% compared to spring and autumn. L&A also identifies less clear-sky moments in winter but unexpectedly does not show more clear-sky moments in summer than in spring and autumn. As written hereafter, the results show that L&A has a tendency to screen-out moments characterised by large *AOT* values which occur more frequently in spring and summer (***Table 3***). Our analysis also shows that in 2018-2019, the accumulated amount of solar radiation (in Wh/m^2) incident under clear-sky conditions (Garcia method) represents 21.2% and 23.7% of the total accumulated *GHI* in Lille, and in Palaiseau, respectively.

The mean solar resource components are quite similar at Lille and Palaiseau, with almost equal $DifHI_{obs}$ values in both all-sky and clear-sky conditions (***Table 2***), indicating comparable impact of the cloud cover. Nonetheless, DNI_{obs} is larger in Palaiseau than in Lille, with a difference of about 30 W/m^2 in all-sky conditions, and approximately 20 W/m^2 in clear-sky conditions. Part of these differences could be attributed to the smaller mean *SZA* in Palaiseau which is located at a lower latitude than Lille. As a consequence, both all-sky and clear-sky GHI_{obs} values are around 25 W/m^2 larger in Palaiseau than in Lille.

Table 2. Averaged solar resource components (GHI_{obs}, DNI_{obs}, $DifHI_{obs}$) observed at Lille and Palaiseau in 2018-2019, in all-sky and in clear-sky conditions, at 1-minute time resolution (SZA < 80°). The all-sky data set corresponds to all data points, while the clear-sky data set is composed by the only minutes identified as cloud-free by either the algorithm of Long and Ackerman [2000] (L&A) or the method of Garcia *et al.* [2014] (Garcia). The second part of the Table gives the number of all-sky minutes, and the proportion (%) of clear-sky minutes, in 2018-2019, as well as for each season.

		Lille			**Palaiseau**		
	Time cover	**All sky**	**Clear sky (L&A)**	**Clear sky (Garcia)**	**All sky**	**Clear sky (L&A)**	**Clear sky (Garcia)**
SZA (°)	**2018–2019 mean ± standard deviation**	59 ± 15	60 ± 14	58 ± 15	58 ± 15	58 ± 14	57 ± 15
GHI_{obs} (W/m^2)		330 ± 252	474 ± 218	493 ± 229	352 ± 264	500 ± 222	516 ± 227
DNI_{obs} (W/m^2)		303 ± 341	765 ± 132	739 ± 144	333 ± 350	784 ± 124	758 ± 139
$DifHI_{obs}$ (W/m^2)		162 ± 108	79 ± 22	92 ± 35	160 ± 107	79 ± 23	93 ± 33
Number of all-sky minutes, and proportion of clear-sky minutes (%)	**2018-2019**	379 717	7.8%	14.2%	427 480	9.8%	16.2%
	Winter	50 446	6.9%	8.3%	67 769	7.4%	8.9%
	Spring	112 195	7.8%	13.0%	125 242	7.9%	13.9%
	Summer	133 665	7.8%	17.9%	142 373	10.5%	20.5%
	Autumn	83 411	8.7%	13.3%	92 096	12.9%	17.9%

As could be expected, the cloud-screening methods agree to show a strong impact in GHI_{obs}, DNI_{obs} and $DifHI_{obs}$, although results vary between the two cloud-screening methods. The influence of the chosen cloud-screening method is more important in DNI_{obs} and $DifHI_{obs}$ than in GHI_{obs}. For example, under clear-sky conditions, $DifHI_{obs}$ is multiplied by a factor of 0.5-0.6 at Lille, DNI_{obs} by a factor of 2.3-2.5, but GHI_{obs} by a factor of ~1.45.

Both cloud-screening methods have a comparable impact in DNI_{obs} at both locations, which increases by 420-460 W/m^2 from all-sky to clear-sky conditions. Conversely, $DifHI_{obs}$ in clear-sky conditions at Lille decreases by 83 W/m^2 with L&A, compared to all-sky, and by 70 W/m^2 with Garcia. In this case, differences in $DifHI_{obs}$ between all-sky and clear-sky conditions is lower for the Garcia cloud-screening method , either due to aerosols or unfiltered clouds. The standard deviation in $DifHI_{obs}$ also strongly decreases from 67% (compared to the average) in all-sky conditions at Lille to 38% in clear-sky conditions with the Garcia method, and to 28% with the L&A method, and in DNI_{obs} from 113% in all-sky to 17-19% in clear-sky. L&A cloud-screening increases GHI_{obs} by ~145 W/m^2 while Garcia cloud-screening increases GHI_{obs} by ~160 W/m^2 at both Lille and Palaiseau. Compared to the L&A method, the Garcia method increases GHI_{obs} by 16-19 W/m^2.

Table 3. Average and standard deviation of instantaneous atmospheric properties measured at Lille and Palaiseau by AERONET in 2018-2019: AOT at 550 nm, the Ångström exponent α, and the water vapour column content (WVC). In clear-sun conditions, the number of observations represents the total number of Level 2.0 AERONET measurements while in clear-sky it corresponds to the number of minutes identified as cloud-free by either the algorithm of Long and Ackerman [2000] (L&A) or the method of Garcia *et al.* [2014] (Garcia), coincident to the Level 2.0 AERONET data.

	Lille			**Palaiseau**		
	Clear-sun (Level 2.0)	**Clear sun & sky (Level 2.0 + L&A)**	**Clear-sun & sky (Level 2.0 + Garcia)**	**Clear-sun (Level 2.0)**	**Clear-sun & sky (Level 2.0 + L&A)**	**Clear-sun & sky (Level 2.0 + Garcia)**
Number of obs.	25 739	7 501	13 189	26 294	9 757	16 156
AOT	0.14 ± 0.10	0.10 ± 0.05	0.13 ± 0.08	0.13 ± 0.08	0.08 ± 0.04	0.11 ± 0.07
α	1.29 ± 0.40	1.34 ± 0.32	1.34 ± 0.36	1.30 ± 0.38	1.30 ± 0.32	1.31 ± 0.35
WVC (cm)	1.5 ± 0.7	1.4 ± 0.5	1.6 ± 0.6	1.6 ± 0.7	1.4 ± 0.5	1.6 ± 0.6

The Level 2.0 AERONET clear-sun data set shows that the aerosol properties and WVC are highly variable in Lille and Palaiseau. The standard deviation is 71% in *AOT* at 550 nm at Lille, 31% in the Ångström exponent α, and 47% in the *WVC* (***Table 3***). A significant part of this variability could be explained by seasonal changes, as mean *AOT* increases by a factor of 1.8 from winter to spring, and mean *WVC* increases by a factor of 3 from winter to summer (Fig. 1). The high variability of *AOT* and *WVC* also relates to intra-seasonal changes. This is particularly noticeable for *AOT*, with a standard deviation in spring remaining close to the standard deviation over a year. The 90th percentile of *AOT* at Lille is 0.32 in 2018-2019. *AOT* could even be larger than 0.80 as on both 2018/06/06 and 2019/03/31. For example a severe aerosol pollution occurred in March 2014, with measured *AOT* reaching values up to 0.90 at Lille and Palaiseau (Dupont et al., 2016, Favez et al., 2021).

The Garcia method keeps the seasonal influence of *AOT* while slightly reducing mean values as well as the standard deviation, mostly in spring-summer (Fig. 1), indicating that some large *AOT* events may be rejected by the cloud-screening. The L&A method however does not keep the seasonal influence of *AOT*, with an increase by only 0.02 from winter to spring, and *AOT* remaining constant from summer to autumn. Moreover the standard deviation is divided by more than 2 in spring-summer. Most large *AOT* events must be rejected by the L&A method. The seasonal dependence of α is not shown as it is not significant.

The annual averages at Lille and Palaiseau are close to the European average according to Gueymard and Yang [2020], based on AERONET, and also close to the average of the Cfb climate zone, embedding both sites [Gueymard and Yang, 2020]. The differences between Lille and Palaiseau are small (Table 3), consistently with Ningombam *et al.* [2019], for the time period 1995-2018. The averaged Level 1.5 AERONET aerosol single scattering albedo at Lille in 2018 is 0.97±0.03 at 440 nm, 0.96±0.04 at 675 nm, and 0.95±0.04 at 870 nm (not shown in Table 3), depicting little absorption.

Our results also suggest that the clear-sky conditions identified by the Garcia cloud-screening method are more representative of the *AOT* variability observed in both Lille and Palaiseau than those detected with the L&A method:

- The number of clear-sky minutes is larger in the Garcia than in the L&A data set (***Table 3***).

- The annual means and standard deviations of *AOT* observed for clear skies identified by the Garcia cloud-screening method are closer to the clear-sun values than those obtained by the L&A method, and especially in spring-summer when L&A significantly underestimates the clear-sun means (***Fig. 1***).

- The relative increase of mean *AOT* from winter to spring for clear skies identified by the Garcia method is close to the increase observed under clear-sun conditions, while variability of AOT is less intense for the situations detected by the L&A method (***Fig. 1***).

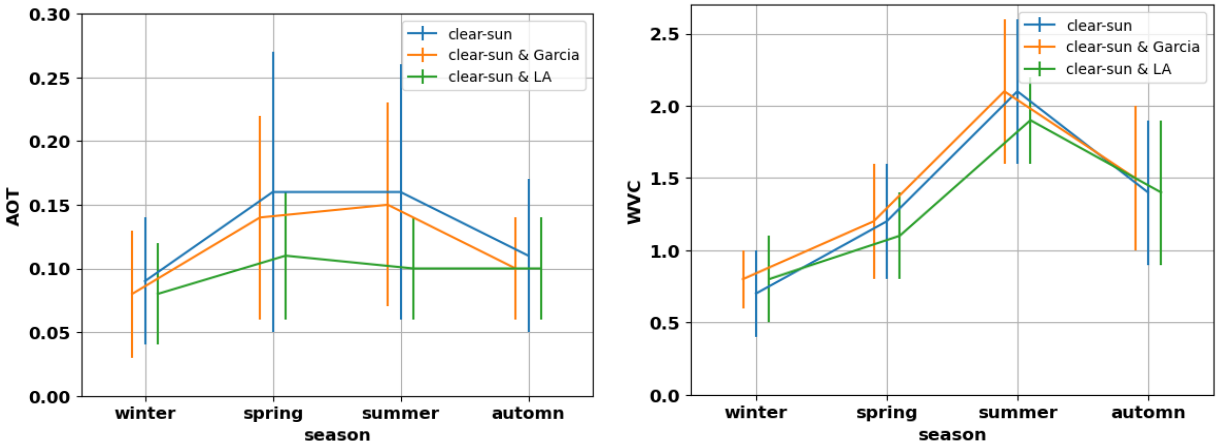

Figure 1. Seasonal dependence of AOT and WVC (cm) at Lille in 2018-2019, according to Level 2.0 AERONET (blue), and for two cloud-screening methods (red for Garcia, green for LA). Vertical bars show the standard deviation for each season.

5. Validation with AERONET as input data

This section presents the comparison scores between SolaRes computations of solar resource standard components (*GHI*, *DNI*, and *DifHI*) and ground-based measurements made at Lille and Palaiseau in 2018-2019. Furthermore, SolaRes computations are also compared to ground-based measurements of *GTI* at Lille in 2019.

Our analysis relies on two main statistical parameters: Comparison the relative mean bias difference (MBD) and the relative root mean square difference (RMSD), which are usual indicators of dispersion, as commented by Gueymard [2014], and used by many authors [e.g. Ruiz-Arias *et al.*, 2013; Sun *et al.* 2019]. *MBD* and *RMSD* values are computed as follows:

$$MBD = \frac{100}{obs_{mean}} \frac{\sum_{i=1}^{N} (comp_i - obs_i)}{N} \quad , \tag{16a}$$

$$RMSD = \frac{100}{obs_{mean}} \left[\frac{\sum_{i=1}^{N} (comp_i - obs_i)^2}{N} \right]^{1/2} , \quad (16b)$$

where obs stands for the observed quantity, and comp for the SolaRes computation, of any solar resource component: *GHI*, *DNI*, *DifHI*, *DifTI*. The sum is made over the pair number N, obs_{mean} stands for the averaged observed quantity, and the factor 100 provides *MBD* and *RMSD* in %. Best agreement between measurements and simulations is reached for the lowest values of MBD and RMSD.

In this section, the continental clean and desert dust OPAC models are mixed to reproduce AERONET spectral *AOT* (***Sect. 3.3***). AERONET V3 provides not only the input spectral *AOT*, but also *WVC*, and the ozone column content. Daily averages of surface albedo delivered by the CAMS-radiation service are used. The 3-minute values are averaged at the 15-minute time resolution. At Lille in 2018-2019, 8500 radiative transfer computations of *DifHI* are performed at the 15-minute time resolution, and are then linearly interpolated at 1-minute resolution. SolaRes provides solar resource components for 183 000 1-minute time steps in clear-sun conditions. Only data within a temporal window of ±10 minutes around the AERONET record time is kept, and the SolaRes data set is then reduced to 125 000 time steps. A further screening is applied on *SZA*, keeping only values smaller than 80°, as done by e.g. Ruiz-Arias *et al.* [2013]. Comparison data pairs are generated by associating coincident simulation and observation at 1-minute time resolution. Eventually, the cloud-screening procedures on solar irradiance measurements (S***ect. 4***) are applied to limit comparisons to clear-sky conditions. Overall, at Lille in 2018-2019, 50 000 comparison data pairs are constituted with the Garcia cloud-screening procedure, and 26 000 comparison data pairs with the L&A cloud-screening procedure (***Table 4***). Slightly more AERONET data are available for radiative transfer computations at Palaiseau over the same years, and more comparison pairs are eventually kept, as ~65 000 pairs with the Garcia cloud-screening method, and 37 000 pairs with the L&A method.

As described in ***Sect. 2.2***, GHI_{obs}, $DirHI_{obs}$ and $DifHI_{obs}$ are measured by four Kipp&Zonen instruments at both Lille and Palaiseau, and GTI_{obs} is measured at Lille by a CMP11 pyranometer in a vertical plane. First, comparisons scores in *GHI* are presented in ***Sect. 5.1***, then comparison scores in both *DNI* and *DifHI*, without (***Sect. 5.2***) and with the circumsolar contribution (***Sect. 5.3***). Finally, Section 5.4 presents the comparison scores obtained for GTI computations on a vertical surface.

5.1. GHI at Lille and Palaiseau

Table 4 and ***Figure 2*** present the comparison scores in *GHI*. Overall, the correlation coefficient between GHI_{obs} and GHI_{RT} is 0.999 for the two sites (Figure 2). For the 'all-seasons' comparison involving the CMP22, GHI_{obs} is slightly underestimated by 0.4% (Palaiseau) to 0.8% (Lille) for clear-skies identified by the Garcia cloud-screening method. The absolute underestimation is -3.8±8.1 W/m^2 at Lille, with 55% of 1-minute values included between -5 and 5 W/m^2, within the uncertainty requirement for the measurements by BSRN [Ohmura *et al.*, 1998]. The *RMSD* in *GHI* is around 1.6% at both Lille and Palaiseau, with the Garcia cloud-screening method.

Table 4. Comparison scores (*MBD* and *RMSD, Eq. 16*) between GHI_{RT} and GHI_{obs}, at both Lille and Palaiseau, for the two cloud-screening procedures (Garcia and L&A as described in ***Sect. 4***), over the whole 2018-2019 period ("all-season"), and for each season. Note that CMP11 measurements of GHI in Lille are limited to spring and summer 2018. The number of comparison pairs (1-minute resolution), and the corresponding averaged GHI_{obs}, are also given.

Location	**Instruments**	**Time period**	**cloud-screening**	**Number of comparison pairs N**	**Mean GHI_{obs} (W/m^2)**	**Comparison scores**	
						MBD (%)	**RMSD (%)**
Lille	CH1+CMP22	All seasons	Garcia	50 000	500±228	-0.8	1.7
		All seasons	L&A	26 000	482±218	-0.5	1.2
		Winter/ spring/ summer/ autumn	Garcia	3 900 / 13 500 / 22 800 / 9 800	324 / 531 / 552 / 409	-0.7/-1.3 / -0.8 / -0.1	1.5 / 1.9 / 1.6/ 1.6
	CMP11	Part of spring+summer 2018	Garcia	7450	538±234	0.0	2.2
Palaiseau	CMP22	All seasons	Garcia	65 400	517±227	-0.4	1.5
		All seasons	L&A	37 500	503±219	-0.1	1.0

The comparison of *GHI* involving the CMP11 at Lille shows a better score in *MBD* and a worst score in *RMSD*, than the CHP1+CMP22 'all-seasons' comparison. The larger *RMSD* involving the CMP11 seems partly correlated with the season. Indeed the *RMSD* obtained with CHP1+CMP22 in spring is 1.9%, which is close to the *RMSD* of 2.2% with the CMP11 in spring-summer, and larger than the all-season *RMSD* of 1.7%.

The smaller *MBD* obtained with the CMP11 pyranometer than with the CHP1+CMP22 combination may be explained by the influence of the different spectral responses of CMP22 and CHP1 on one side, and of CMP11 on the other side. Indeed according to SolaRes, the shorter CMP11 spectral bandwidth of the CMP11 reduces GHI_{RT} by around 4.5±2.5 W/m^2, or 0.8±0.3%. This mean decrease of GHI_{RT}, added to the mean negative bias obtained with the CHP1+CMP22 combination, is close to the observed difference of 1.6% between CMP11 and CHP1+CMP22 GHI_{obs} (***Sect. 2.2***). Consequently, MBD becomes negligible when comparing SolaRes estimates with CMP11 measurements. T

Our results also show that the cloud-screening method has a significant impact on the comparison scores. For example on 20 April 2018 between 12:00 and 14:00 at Lille, the largest disagreement in *GHI* occurs between the measurements and the SolaRes computations, with values reaching 60 W/m^2 (***Fig. 3***). It is however limited to the Garcia method, as the L&A screening procedure gets rid of these points, consistently with its lower FPS by Gueymard *et al.* [2019]. AERONET Level 2.0 provides values of *AOT* all day, meaning that no clouds are seen in the solar direction, and satisfying agreement in *DNI* indeed occurs between 12:00 and 14:00 (Fig. 3 middle). However significant disagreement occurs in *DifHI*, which is the cause of disagreement in GHI, suggesting the presence of clouds in the sky vault, but undetected by the Garcia cloud-screening method. Such a behaviour also happens twice later in the afternoon, with less intensity. During these 3 occurrences, the aerosol influence is well reproduced as we find agreement in *DNI*, and *DifHI* is systematically underestimated because of cloud presence in the sky vault (Fig. 3).

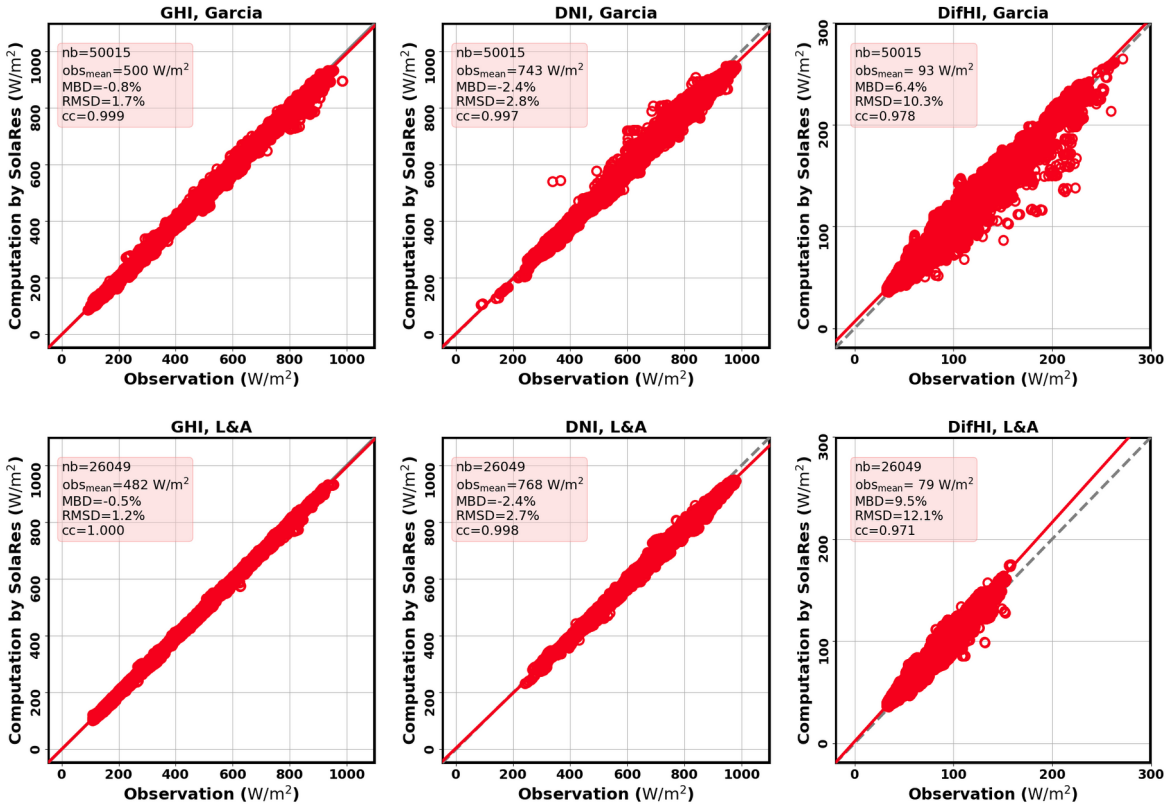

Figure 2. Comparison between 1-minute computations and observations at Lille in 2018-2019 (by CHP1+CMP22) in clear-sky conditions, for *GHI* (left), *DNI* (centre), and *DifHI* (right). Clear-skies are identified by both by the Garcia (top) and the L&A cloud-screening methods (bottom). Only comparison pairs with *SZA* < 80°, and within 10 minutes of AERONET record time of *AOT* are considered. *MBD* and *RMSD* are given according to ***Eq. 16***, *nb* is the number of pairs, obs_{mean} is the mean value of the observed solar resource component, and cc is the correlation coefficient of the linear interpolation (red line). The dashed grey line represents the 'x=y' line.

Such a behaviour has consequences on the mean comparison scores over the full time period, as MBD and RMSD values decrease when considering only clear-skies identified by the L&A cloud-screening procedure (***Table 4 and Fig. 2***). In particular, the L&A cloud-screening procedure decreases *MBD* in *GHI* by ~0.3%, and *RMSD* by ~0.5%. *MBD* even reaches values as low as -0.1% at Palaiseau with L&A, with 64% of the *MBD* values lying within ±5 W/m^2 of GHI_{obs}. *RMSD* could be as low as 1.0%, confirming the success of the radiative closure study involving pyranometers, AERONET *AOT* and SolaRes.

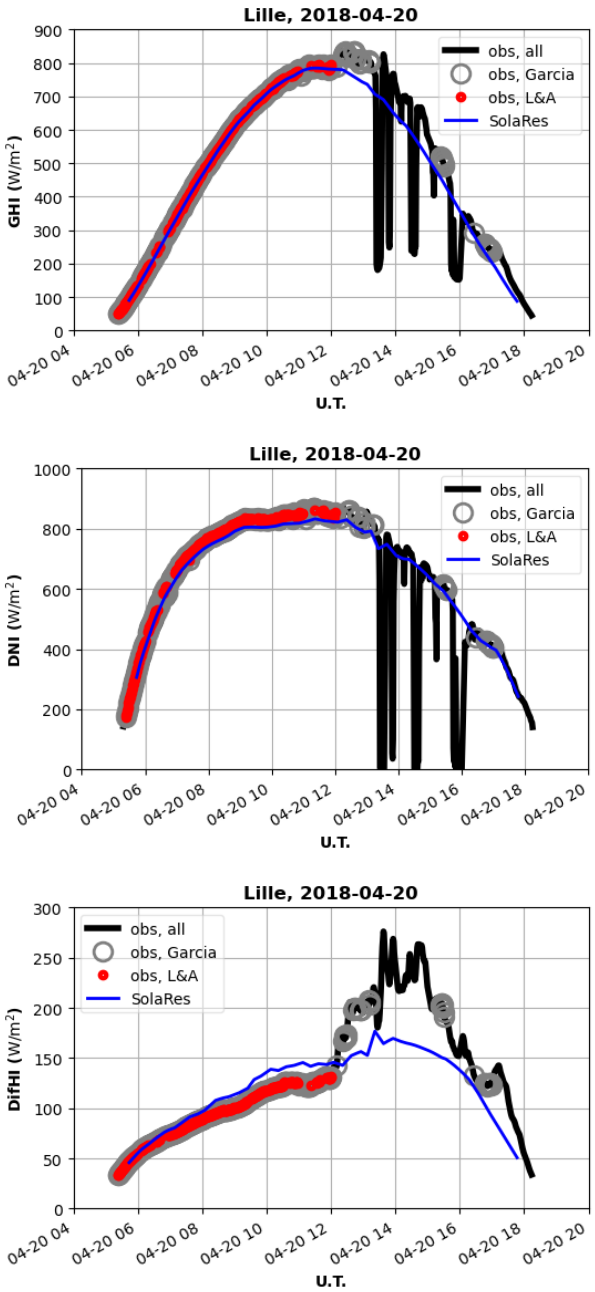

Figure 3. GHI (top), DNI (middle), and DifHI (bottom) observed (black line) at Lille on 2018/04/20, and also simulated by SolaRes (blue line). GHI_{obs} is cloud-screened by both Garcia (grey circles) and L&A methods (red dots).

5.2. DNI and DifHI without the circumsolar contribution

Both DNI_{obs} and $DifHI_{obs}$ are separately measured at Lille and Palaiseau by the CHP1 pyrheliometer and the shaded CMP22 pyranometer, respectively. ***Tables 5 and 6*** present the comparison scores for *DNI* and *DifHI*, respectively, as well as ***Fig. 2*** (centre and right columns). In this section, the circumsolar contribution is not computed, DNI_{strict} is compared to DNI_{obs}, and $DifHI_{strict}$ to $DifHI_{obs}$.

Overall, DNI_{strict} is underestimated by -1.6% at Palaiseau and -2.4% at Lille (***Table 5 and Fig. 2***) with the Garcia cloud-screening method, and *RMSD* is 2.2% at Palaiseau and 2.8% at Lille. These

results are highly satisfactory given the 5% uncertainty in *DNI* claimed by Gueymard and Ruiz-Arias [2015] for uncertainty of 0.02 in *AOT (of AERONET measurements).*

We can confidently guess negligible residual cloud influence in the solar direction as AERONET Level 2.0 screens out clouds in the solar direction, and it is associated with the solar irradiance cloud-screening methods. The dependence of the comparison scores in DNI on the cloud-screening procedure is small, as the criteria on direct solar irradiance are similar between the two cloud-screening procedures. The different *AOT* ranges between the two cloud-screening methods do not affect the comparison scores.

While DNI_{strict} is underestimated, $DifHI_{strict}$ is overestimated, with MBD values of around 6% at Lille and Palaiseau for clear skies identified with the Garcia cloud-screening method (***Table 6 and Fig. 2***). According to ***Eq. 10*** and ***11***, both DNI_{obs} underestimation and $DifHI_{obs}$ overestimation are expected, as the circumsolar contribution is not considered here.

RMSD in *DifHI* is found to be of the order of 10% at both stations, which is significantly larger than *RMSD* in both *GHI* and *DNI*. Better results in *DNI* than in *DifHI* are to be expected as *AOT*, which is the main input parameter of SolaRes, exclusively informs on aerosol extinction and mean size but neither on the proportion between scattering and absorption, nor on surface reflection, which are both factors of *DifHI* but not of *DNI*. Moreover, uncertainty also arises from the interpolation procedure between 15-minute estimates of *DifHI* with SMART-G. Eventually, the better agreement in *GHI* (***Sect. 5.1***) than in both *DNI* and *DifHI* shows that *MBD* in both *DNI* and *DifHI* mostly compensates.

Table 5. As ***Table 4***, but for DNI_{obs} measured by the CHP1 pyrheliometer.

Location	Time period	cloud-screening	Circumsolar contribution simulated	Comparison pair numbers	Mean DNI_{obs} (W/m^2)	Comparison scores	
						MBD (%)	RMSD (%)
Lille	Whole year	Garcia	no	50 000	743±141	-2.4	2.8
	Whole year	L&A	no	26 000	768±120	-2.4	2.7
	Whole year	Garcia	yes	50 000	743±141	-1.2	2.2
	Winter/spring/ summer/autumn	Garcia	no	3 900 / 13 500 / 22 800 / 9 800	742 / 757 / 737 / 737	-2.0 / -2.5 / -2.5 / -2.4	2.6 / 2.8 / 2.8 / 2.9
Palaiseau	Whole year	Garcia	no	65 400	758±139	-1.6	2.2
	Whole year	L&A	no	37 500	785±123	-1.6	1.8
	Whole year	Garcia	yes	65 400	758±139	-0.5	1.8

It may be surprising that *MBD* in *DifHI* increases with the L&A cloud-screening procedure. This could be partly explained by the significant decrease in mean *DifHI*, as L&A screens out atmospheric conditions with largest *AOT*, and thus cases of higher diffuse irradiance. Similarly, *MBD* is significantly smaller in spring-summer than in autumn-winter, due partly to higher mean *DifHI* values.

Both mean GHI_{obs} and mean $DirHI_{obs}$ are much larger at Palaiseau according to Gschwind *et al.* [2019] than with our cloud-screening procedures: GHI_{obs} averaged over 2005-2007 is 600 W/m^2, and mean $DirHI_{obs}$ is 492 W/m^2 with a strict cloud-screening procedure keeping only ~10 000 1-minute data per year. Consequently, $DifHI_{obs}$ is 108 W/m^2 for Gschwind *et al.* [2019], also larger

than with our cloud-screening procedures. Indeed, annual mean GHI_{obs} varies between 500 and 517 W/m^2 in 2018 and 2019 at Palaiseau, and $DifHI_{obs}$ between 79 and 93 W/m^2, with (Tables 4 and 6) and without AERONET cloud-screening (Table 2). According to ***Table 2***, $DirHI_{obs}$ is ~420 W/m^2, subtracting $DifHI_{obs}$ to GHI_{obs}.

Table 6. Same as ***Table 4***, but for $DifHI_{obs}$, measured by the CMP22 pyranometer in 2018-2019.

Location	Time period	cloud-screening	Circumsolar contribution simulated	Comparison pair number	Mean $DifHI_{obs}$ (W/m^2)	Comparison scores	
						MBD (%)	RMSD (%)
Lille	Whole year	Garcia	no	50 000	93±35	6.4	10.3
	Whole year	L&A	no	26 000	79±22	9.5	12.1
	Whole year	Garcia	yes	50 000	93±35	2.4	9.4
	Winter/spring/ summer/autumn	Garcia	no	3 900 / 13 500 / 22 800 / 9 800	62 / 99 / 102 / 77	7.0 / 5.6 / 6.4 / 7.5	9.4 / 9.8 / 10.2 / 11.1
Palaiseau	Whole year	Garcia	no	65 400	92±33	5.1	10.0
	Whole year	L&A	no	37 500	80±23	7.5	10.0
	Whole year	Garcia	yes	65 400	92±33	1.3	9.3

As shown in ***Sect. 4***, when the cloud-screening is stricter, atmospheric scattering is reduced, and $DifHI_{obs}$ may decrease, while on the contrary DNI_{obs} may increase. As the Gschwind *et al.* [2019] data filtering increases both $DifHI_{obs}$ and $DirHI_{obs}$, the cloud-screening strictness is not in play. Another important factor is *SZA*. We could then make the hypothesis that the Gschwind *et al.* [2019] data filtering procedure rejects large values of *SZA*, such as mean *SZA* would be smaller than in our data sets (***Table 2***), explaining the increase in both $DirHI_{obs}$ and $DifHI_{obs}$ and consequently in GHI_{obs}.

5.3. DNI and DifHI with the circumsolar contribution

In this Section, we consider DNI_{pyr} and $DifHI_{pyr}$, which are corrected by the circumsolar contribution to better represent the measurements, according to ***Eq. 10*** and ***11***. The circumsolar contribution to the direct normal radiation, $\Delta DifNI_{circ}$, is found to be 8±6 W/m^2 on average (similar on both sites), with a median and a 90th percentile of 6 and 15 W/m^2, respectively. $\Delta DifNI_{circ}$ then represents 1.2±1.3% of DNI_{strict}, with a median of 0.7%, and a 90th percentile of 2.4%. ***Figure 4*** shows $\Delta DifNI_{circ}$ in function of both the Ångström exponent α and the slant aerosol optical thickness at 550 nm (SOT) which is defined as *AOT* divided by μ_0 [Blanc *et al.*, 2014]. Most values of $\Delta DifNI_{circ}$ are smaller than 20 W/m^2, consistently with simulations by Blanc *et al.* [2014]. Values larger than 20 W/m^2 mostly occurs for small α and/or large *SOT*.

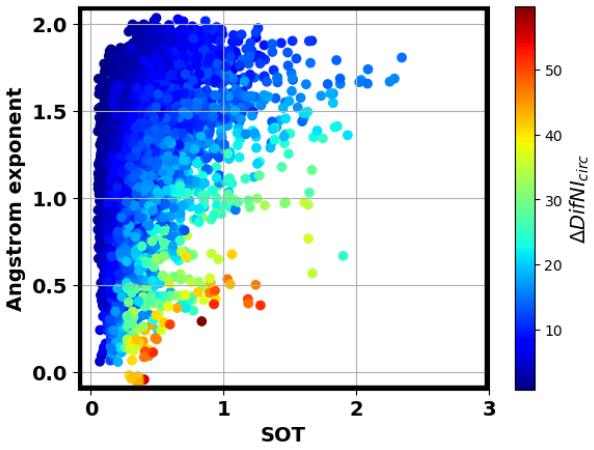

Fig. 4. The circumsolar contribution $\Delta DifNI_{circ}$ (W/m^2) in function of both the Ångström exponent α and the slant path optical thickness at 550 nm (SOT) at Lille in 2018.

Overall, adding $\Delta DifNI_{circ}$ to DNI_{strict} improves the comparison scores, with a decrease of both *MBD* and *RMSD* in *DNI*, by more than 1%, and ~0.5%, respectively (Table 5). The mean circumsolar contribution to diffuse horizontal irradiance, $\Delta DifHI_{circ}$, is 4±2 W/m^2, and the comparison scores with $DifHI_{pyr}$ also significantly improve, with *MBD* decreasing by more than 4% and RMSD slightly decreasing by less than 1% (Table 6).

5.4. Diffuse irradiance in a vertical plane

5.4.1. Two regimes

GTI_{obs} is measured at Lille from 2019/01/18 to 2019/12/31 by the CMP11 pyranometer, the instrument being tilted vertically at 90° and facing southward (i.e. azimuth angle of 180°). Signal in summer shows two distinct regimes, as for example on the 27th of June 2019 (***Fig. 5***):

1. Most of the day around noon, the sun, positioned in the southern half-sky, faces the instrument, and is thus included in the instrument field of view. Both diffuse and direct radiation are then observed.

2. At both beginning and end of the day, the sun could be positioned behind the instrument in the northern half-sky, the instrument sensor then being in shadows. Only diffuse radiation is observed, which is less dependent on SZA than direct radiation, generating the flatter wings at the end of the day than around noon.

Comparisons are made in both regimes independently.

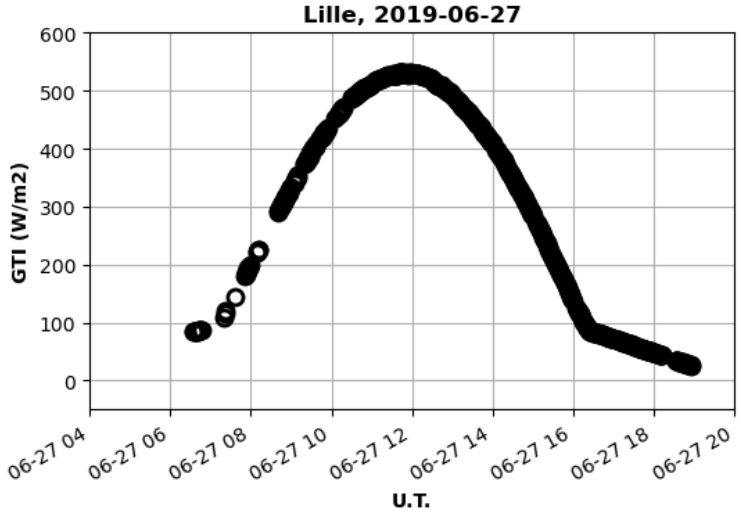

Figure 5. Global tilted irradiance (GTI_{obs}) observed by the CMP11 pyranometer in a vertical plane facing South, on 2019/06/27 at Lille. The sun is southwards between 07:14 and 16:27.

5.4.2. Diffuse contribution at both beginning and end of the day in summer

Comparison of *GTI* between observations and SolaRes simulations is made by selecting *SAA* larger than 270° (end of the day in summer). Around a thousand comparison pairs are generated. Overall, observation tends to be overestimated by 6% and the *RMSD* is 8.5% (1st line in ***Table 7***). similarly, by selecting *SAA* smaller than 90° (beginning of the day), the overestimation is 8.7% and the *RMSD* is 12.1%. These results are similar to the comparison scores in *DifHI* (***Table 6***).

Table 7. Same as ***Table 4*** but for *GTI* in the vertical plane facing South at Lille in 2019, for clear skies identified with the Garcia cloud-screening procedure. The time period is defined by season and by the range of *SAA*. Computations are also made for different values of the surface albedo.

Time period	Surface albedo	Comparison scores		
		Number of comparison pairs	MBD (%)	RMSD (%)
SAA > 270° (only summer)	0.13	1109	6.0	8.5
SAA < 90° (only summer)	0.13		8.7	12.1
90 < SAA < 270°	0.13	18 655	-0.6	5.0
90 < SAA < 270°, summer	0.13	9395	3.7	4.9
90 < SAA < 270°, winter	0.13	2654	-6.5	6.8
90 < SAA < 270°, winter	0.35	2654	-0.2	1.4

5.4.3. The influence of changing surface albedo on GTI

Comparison between observation and simulation for the sun facing the instrument (90° < *SAA* < 270°) shows that GTI_{obs} can be accurately reproduced but with an *RMSD* of 5% (2nd line in ***Table 7***).

The overall larger *RMSD* in *GTI* than in *GHI* (***Table 4***) is partly caused by the variability in the effective surface albedo.

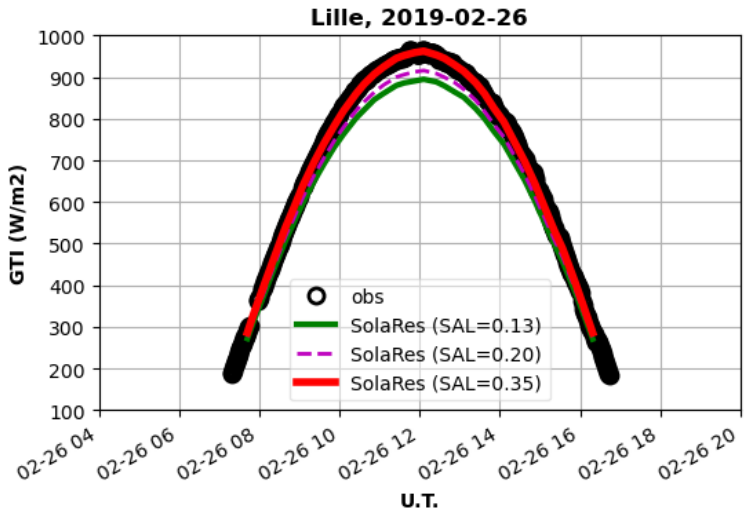

Figure 6. Same as ***Fig. 5*** but for 26/02/2019, and with SolaRes estimates for different values of the surface albedo (SAL). According to MODIS, the daily average of the surface albedo is 0.13.

By distinguishing winter and summer seasons, *MBD* changes from +3.7% in summer to -6.5% in winter (3rd and 4th lines in ***Table 7***). Although changes in the surface albedo derived from satellite observations appear to be small, computations for the 26th of February 2019 shows that observations can be reproduced with an effective surface albedo of 0.35 (***Fig. 6***), explaining the underestimation of 6.5%. The underestimation in winter then decreases from 6.5% to 0.2%, and *RMSD* reaches decreases down to 1.4% (6th line in ***Table 7)***, which is similar to results in *GHI* (***Table 4***). Heterogeneities in the albedo of building's walls at local scale, and subsequent 3D effects, could be responsible of such differences between a satellite surface albedo and an effective surface albedo for a vertical instrument. The differences between winter and summer seasons could be caused by fallen leaves of surrounding trees, in relation with the sun position in the sky. Consistently to our results, Mubarak [2017] also show that the surface albedo has a significant effect on estimating *GTI* in a vertical plane (but with a transposition model).

6. Influence of the aerosol parameterisation and the data source

This section shows the sensitivity of the computed solar resource parameters to the parameterisation of the aerosol properties and also to the aerosol data source.

Atmospheric optical properties are necessary input data of a radiative transfer code. In clear-sky conditions, aerosols are the main source of variability of the atmospheric optical properties. Necessary aerosol optical properties are the optical thickness, the phase function and the single scattering albedo at any wavelengths. Measurements are exploited to reproduce the temporal variability in aerosol optical properties. However, measurements can rarely provide all necessary optical properties, as the full phase function and the single scattering albedo. It is therefore necessary to employ various strategies to get the necessary parameters from observation data sets. For example the measured data set can be inverted to provide a fully-described microphysical aerosol model, assuming some hypotheses, which is then usable in radiative transfer computations.

AERONET provides such inverted aerosol models, at a resolution of around 1 hour. For the validation, we prefer relying on the highest sampling rate by AERONET, at three minutes, which detects and best describes most aerosol events, with spectral *AOT*. *AOT* measured at the two wavelengths of 440 and 870 nm is used to constrain the mean aerosol burden and also as an indicator of the mean aerosol size. Two aerosol OPAC models are mixed in such proportions that they reproduce the observed *AOT* (**Eq. 13**). and all necessary aerosol optical properties. First, performances of SolaRes computations are compared for various combinations of the OPAC aerosol models (***Sect. 6.1***). The influence of the input data source is also evaluated by testing the CAMS-NRT regular-grid global data set as input data of SolaRes (***Sect. 6.3***).

6.1. Impact of the aerosol parameterisation: the aerosol model combination

wavelengths. While validation in ***Sect. 5*** is performed with a mixture of continental clean and desert dust aerosol OPAC models, the aerosol models are changed here to show the sensitivity of the solar resource parameters on the aerosol parameterisation. To best reproduce the observed *AOT* spectral variability, an aerosol model mainly composed by relatively small aerosols (producing large α) is mixed with an aerosol model composed by larger aerosols (producing small α). The large-α aerosol models are named by OPAC as continental clean, continental polluted, and urban, and the small-α aerosol models are named desert dust, maritime clean, maritime polluted. ***Table 8*** shows the impact of several aerosol model combinations on the comparison scores between observation and simulations, which include the circumsolar contribution. In this subsection, only clear-sky moments identified by the Garcia cloud-screening method are selected at Lille in 2018.

DNI_{pyr} is the least sensitive parameter to the various combinations of aerosol models, with *MBD* changing between -1.3 to -1.7%, and *RMSD* remaining around 2.5% (***Table 8***). This low sensitivity is expected as only the circumsolar contribution in DNI_{pyr} depends on the angular scattering and on the absorption of solar radiation, which is relatively small at Lille (~1%). $DifHI_{pyr}$ does however depend on both the phase function and the single scattering albedo, and is thus much more dependent on the aerosol models than DNI_{pyr}. The mean absorption coefficient increases from continental clean to continental polluted and to the urban model, leading to a decrease of $DifHI_{pyr}$, and to a significant decrease of *MBD* from ~+3% (continental clean) to ~-12% (urban). In contrast, the small-α model shows less influence than the large-α model (***Table 8***).

Table 8. Sensitivity of the solar resource components to the OPAC aerosol models, in terms of *MBD* and *RMSD* in *GHI*, DNI_{pyr}, and $DifHI_{pyr}$. As large-α models, *cc* stands for continental clean, *cp* for continental polluted and *ur* for urban. As small-α models, *dd* stands for desert dust, *mc* for maritime clean and *mp* for maritime polluted. Comparisons are made with observations made in 2018 at Lille, for clear skies identified by the Garcia cloud-screening method.

Aerosol models	**GHI**		**DNI_{pyr}**		**$DifHI_{pyr}$**	
	MBD (%)	**RMSD (%)**	**MBD (%)**	**RMSD (%)**	**MBD (%)**	**RMSD (%)**
cc_dd	-0.7	1.8	-1.0	2.4	2.2	10.3
cp_dd	-2.2	3.0	-1.6	2.5	-4.1	12.3
ur_dd	-3.7	4.7	-1.7	2.5	-12.3	19.9
cc_mc	-0.7	1.8	-1.3	2.4	3.1	10.4
ur_mc	-3.6	4.9	-1.7	2.5	-11.7	20.6
cc_mp	-0.6	1.7	-1.3	2.4	3.3	10.4

ur_mp	-3.3	4.1	-1.8	2.5	-8.4	16.4

As a result, the aerosol model mixture significantly affects *GHI* simulations, mainly because of the sensitivity of $DifHI_{pyr}$ to the large-α aerosol model. The efficient compensation between DNI_{pyr} underestimation and $DifHI_{pyr}$ overestimation mostly occurs with the continental clean (cc) model, which provides the best scores in *GHI*, with an *MBD* of -0.7% and an *RMSD* of 1.8% in 2018 at Lille. This is consistent with the large value of averaged *SSA* at Lille in 2018, as inverted from AERONET measurements.

The choice of the small-α aerosol model has little influence on *GHI*. It is pertinent to chose desert dust as it can be transported to Europe from North Africa [Papayannis *et al.*, 2008].

6.2. Impact of the aerosol parameterisation: the AERONET-inverted aerosol optical properties as data source instead of spectral AOT

In this subsection, the AERONET-inverted aerosol model is exploited by SolaRes, replacing the spectral AOT parameterisation. AERONET

The time resolution of the the AERONET-inverted aerosol model is around 1 hour, and 420 time records are available in 2018 at Lille, instead of the ~13 000 Level 2.0 *AOT* time records. As with the AOT reparametrisation, computations are interpolated at 1-minute, but the ±10 minute condition is not applied here, in order to get as many 1-minute data pairs as possible.

Table 9 shows the comparison scores between observations and simulations for *GHI*, DNI_{pyr} and $DifHI_{pyr}$. The *RMSD* in *GHI* decreases from 1.7 to 1.2% with Garcia, and from 1.2 to 0.8% with L&A (compared to scores in Table 4), while *MBD* becomes negligible for both cloud-screening methods. Ruiz-Arias *et al.* [2013] also compare observation and computations exploiting Level 1.5 AERONET inverted products with a radiative transfer code, but for smaller mean *AOT*. In *GHI*, our performances are similar to Ruiz-Arias *et al.* [2013] comparison scores, with *RMSD* of ~1% and *MBD* of 0%. Such a high performance is also attained with the AERONET spectral *AOT* parameterisation at Palaiseau, and the L&A cloud-screening method (Table 4). We demonstrate the high performance of SolaRes in *GHI* with the 1-minute resolution over at least a year, making SolaRes consistent with scientific and industrial applications. Ruiz-Arias *et al.* [2013] also show significant spatial variability of the comparison scores, with *MBD* changing from 0 to -1% depending on the site. Similarly, ***Sect. 5.1*** also presents 0.4% difference in *MBD* between Lille and Palaiseau.

The performances in DNI do not significantly improve with the AERONET-inverted models, showing that the simpler approach based on spectral *AOT* is appropriate to get high precision in DNI_{pyr} (Table 5). method. Ruiz-Arias *et al.* [2013] present *MBD* of 0%, but which would be expected negative as no circumsolar contribution is computed. The *RMSD* in DNI_{pyr} with SolaRes is twice larger than presented by Ruiz-Arias *et al.* [2013], but for larger mean *AOT* at Lille and Palaiseau than on their data sets.

The AERONET-inverted aerosol model slightly improves $DifHI_{pyr}$ simulations. Moreover MBD remains positive, which is in agreement with the tendency of overestimation shown by Ruiz-Arias *et al.* [2013]. In addition Ruiz-Arias *et al.* [2013] also showed spatial variability of comparison scores and our scores for $DifHI_{pyr}$ are similar to what is presented for one of their sites, but where mean *AOT* is smaller than at Lille in 2018. As the inverted AERONET aerosol model is expected to be the best model, the remaining discrepancies could be linked to other sources, as notably the surface reflection model in SolaRes. According to AERONET inversion products, the surface albedo at Lille at 440 and 675 nm are smaller than what is used in the present study. Reducing the

surface albedo should indeed reduce *DifHI*, as well as the *MBD*. However, studying the sensitivity on surface albedo is beyond the scope of this paper.

Table 9. Same as ***Table 4*** but for *GHI*, DNI_{pyr} and $DifHI_{pyr}$, at Lille in 2018. The AERONET inverted aerosol model composes the input data set of SolaRes.

Solar resource parameter	Cloud-screening method	Number of comparison pairs	Mean solar resource parameters (W/m^2)	Comparison scores	
				MBD (%)	RMSD (%)
GHI	Garcia	26 500	581±193	0.2	1.2
	L&A	14 200	544±184	0	0.8
DNI_{pyr}	Garcia	26 500	779±105	-1.2	2.0
	L&A	14 200	808+-83	-1.4	1.8
$DifHI_{pyr}$	Garcia	26 500	105±40	7.1	9.5
	L&A	14 200	82±16	8.2	10.4

6.3. Impact of the input data source: reanalysis global data set

AERONET provides observations of columnar aerosol optical properties with the best precision and accuracy. However, the AERONET data sets are site-specific and present limited spatial coverage of the Earth, despite an increasing number of stations. To provide solar resource parameters anywhere on the globe, it is necessary to use a global data set defined on a regular grid and on a constant time step, such as provided by global transport and chemistry models used in the CAMS and Modern-Era Retrospective Analysis for Research and Applications, Version 2 (MERRA-2) [Gelaro *et al.*, 2017] programs. Compared to AERONET, such data sets exhibit large uncertainties [Gueymard *et al.*, 2020], it is consequently important to evaluate their influence on the computed solar resource components (*GHI*, *DNI*, *DifHI*).

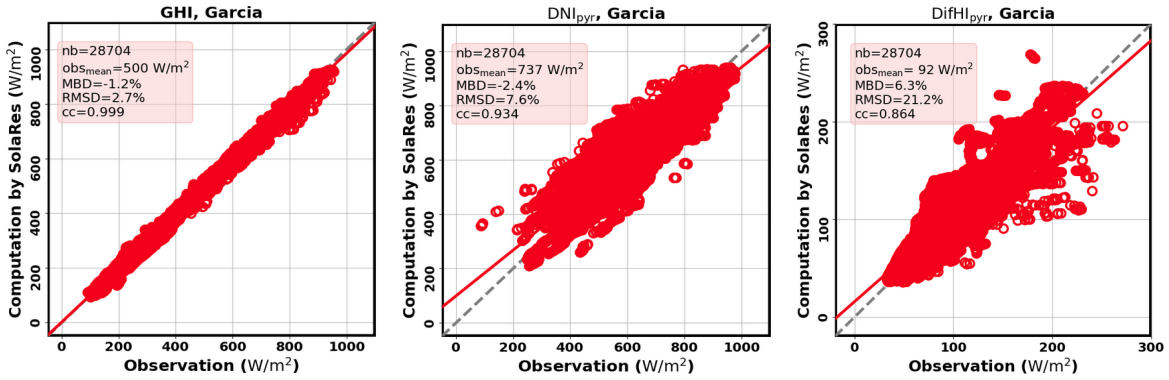

Figure 7. Same as ***Fig. 2*** for solar resource parameter comparisons at Lille but for CAMS-NRT as input data source instead of AERONET, with the Garcia cloud-screening procedure applied in 2018 (no AERONET cloud-screening). *GHI*, DNI_{pyr} and $DifHI_{pyr}$ are showed.

Comparison between observations and simulations is performed at Lille in 2018 with CAMS-NRT (***Sect. 2.4***) instead of AERONET. The cloud-screening is now based uniquely on solar irradiance measurements, and not on the AERONET Level 2.0 clear-sun method. As expected, SolaRes simulations present higher *RMSD* values for all solar resource components with CAMS-NRT than with AERONET. *RMSD* in *GHI* increases by 0.6 to 0.8%, to reach 2.7% with the Garcia cloud-

screening (***Fig. 7***), and 1.8% with the L&A cloud-screening (not shown). The cloud-screening influence is found to be 0.9% with CAMS-NRT data set, when it is 0.5% with the AERONET spectral *AOT* parameterisation (***Sect. 5.1***).

The impact is larger in DNI_{pyr} and $DifHI_{pyr}$, with *RMSD* in DNI_{pyr} increasing by ~5% to reach 7.6%, and *RMSD* in $DifHI_{pyr}$ increasing by more than 10%. This is consistent with Ruiz-Arias *et al.* [2013] stating that: *"the impact of aerosols in direct surface irradiance is about three to four times larger than it is in global surface irradiance"*, quoting Gueymard [2012]. Test was done by adding the Level 2.0 AERONET clear-sun method, reducing *RMSD* in DNI_{pyr} by only 0.3%. Witthuhn *et al.* [2021] shows that the increased *RMSD* for both *GHI* and *DNI* is caused by the dispersion of CAMS *AOT* compared to AERONET. Their results over Germany in 2015 are similar to ours, with *RMSD* values of 3.2%, 8.6% and 15.2% in *GHI*, *DNI* and *DifHI*, respectively, using CAMS reanalysis and a different cloud-screening procedure. Note however that their results show an overestimation of the simulated *DNI* compared to observations, on contrary to SolaRes results. Also, Salamalikis et al. [2021] evaluate a 7.7% *RMSD* in *DNI* caused by CAMS reanalysis *AOT* compared to AERONET *AOT*, in Western Europe, when we have a 5% increase. The *RMSD* between observations and SolaRes *GHI* remains smaller than the best score of 3.0% provided by Sun *et al.* [2019] for many sites. The main differences with our comparison study, is that Sun *et al.* [2019] use the MERRA-2 data set instead of CAMS-NRT. Also, their scores are obtained for a much larger observation data set, more representative of the global variability of aerosol properties than the measurements of Lille and Palaiseau.

7. Conclusion

The SolaRes tool, based on the radiative transfer code SMART-G, aims to estimate solar resource components with precision and accuracy anywhere on the globe, for a variety of meteorological and ground surface conditions, and for any solar plant technology. SolaRes is designed for a large number of scientific to industrial applications, by producing time series at 1 minute time resolution and covering all situations for more than a year, with acceptable computational speed. Input parameters are atmospheric optical properties as the spectral aerosol and cloud optical thickness, which are usually available in many data sets.

As a first step in the comprehensive validation process, this paper evaluates SolaRes retrievals in clear-sky conditions by comparison to ground-based measurements of surface solar irradiance from 2 sites of north of France . This approach aims to asses the main roles of aerosols, whose influences dominate in the absence of clouds, when *GHI* and *DNI* are maximum Aerosol and water vapour parameters can be measured coincidently and precisely by the ground-based instrumentation of AERONET, and the validation in clear-sky conditions is then a radiative closure study.

We perform comparisons between SolaRes estimates and two years (2018-2019) of ground-based measurements of the solar resource components (*GHI*, *DNI*, *DifHI*) at Lille (ATOLL) and Palaiseau (BSRN site) at 1 minute time resolution. GHI_{obs} is slightly underestimated by SolaRes (0.1%) with a mean *RMSD* of around 1.0% at Palaiseau, when a strict cloud-screening method is applied, based on Long and Ackerman [2000] (L&A), but also filtering conditions with largest *AOT*, as those occurring in spring and summer. Another cloud-screening method based on Garcia *et al.* [2014] (Garcia thereafter) is used which is more representative of the aerosol variability conditions. With this cloud-screening method, underestimation slightly worsens to 0.4% at Palaiseau and 0.8% at Lille, partly because of residual clouds increasing *DifHI*, and *RMSD* increases to ~1.6%. Thereafter, when not mentioned, results are given with the Garcia cloud-screening method, which is more representative of the aerosol conditions over northern France.

SolaRes is able to consider various spectral bandwidths, and results are found similar with another instrument operating in a slightly restricted spectrum. SolaRes also performs well to reproduce the angular features of the solar radiation field. The comparison scores in both *DNI* and *DifHI* improve by considering the circumsolar contribution. Indeed, underestimation of DNI_{obs} by SolaRes decreases by 1% to reach an *MBD* of -1.0%, by considering the circumsolar contribution, and the *RMSD* also slightly decreases to reach ~2%. Overestimation of *DifHI* by SolaRes decreases by ~4% to reach an *MBD* of 3% at Lille and 2% at Palaiseau, with an *RMSD* of 10%. It is interesting to note that *DNI* underestimation and *DifHI* overestimation mostly compensate to provide mean overall agreement in *GHI*.

The advantages of using SolaRes for solar resource estimates with tilted panels is twofold: 1) *DNI* and *DifHI* are correctly computed, even considering the circumsolar contribution for comparison purposes with observation; 2) *DifTI* can be computed by radiative transfer computations, then avoiding uncertainties arising with transposition models [i.e. Mubarak *et al.*, 2017]. Comparisons with measurements performed in a vertical plane facing South show satisfying agreement for *DifTI* with an *RMSD* of 8%. It is suggested a strong influence of reflection by not only ground surface but also surrounding buildings, and changing with the season. Indeed, *GTI* measured exclusively in winter could be reproduced with same scores as *GHI* but with a surface albedo increased from 0.13 to 0.35.

Input spectral *AOT* allows to constrain both mean aerosol extinction and size, but neither the aerosol absorption nor the angular behaviour of aerosol scattering. Hypothesis is then necessary to complement the aerosol model in order to perform radiative transfer computations. Two aerosol models of the OPAC database are combined to reproduce input spectral *AOT*, which are modified to study their influence on the solar resource parameters. Input spectral *AOT* efficiently constrains *DNI*, as *DNI* is little sensitive to the aerosol models. However *DifHI* is highly sensitive to the aerosol models. Indeed SolaRes *DifHI* significantly decreases with increasing aerosol absorption of the aerosol model, and *MBD* in *DifHI* becomes negative with urban aerosols instead of continental clean aerosols. Consequently *GHI* underestimation could worsen to 2% and *RMSD* in *GHI* could increase to 4%. We found that the best combination at Lille and Palaiseau consists in a continental clean aerosol model mixed with a desert dust model. Further tests with the aerosol models inverted by AERONET show significant improvement in *GHI*, by decreasing *MBD* to 0.2% and by decreasing *RMSD* by 0.5%. *RMSD* in *GHI* could even be smaller than 1% at Lille with the L&A cloud-screening. In conclusion, SolaRes can reproduce *GHI* at 1-minute resolution, with negligible bias and *RMSD* smaller than 1%, with appropriate input data on aerosols, which is spectral *AOT* at Palaiseau or AERONET-inverted model at Lille. With a cloud-screening method keeping larger values of *AOT*, *MBD* remains smaller than 0.5% and *RMSD* smaller than 1.5%.

Comparisons are also done in the SolaRes global mode, by using input *AOT* and *WVC* delivered by CAMS-NRT instead of AERONET. The *RMSD* in *GHI* increases by 0.6-1.0%, and becomes 1.8% with the L&A cloud-screening and 2.7% with the Garcia cloud-screening. The *RMSD* in *DNI* increases by ~5%, and the *RMSD* in *DifHI* increases by more than 10%. Scores also depend on the site, as RMSD in GHI is smaller by ~0.2% at Palaiseau than at Lille, and MBD by 0.4%. The combined irradiance and AERONET cloud-screening methods also show that there are ~2% more clear-sky conditions at Palaiseau than at Lille, that *AOT* is smaller by ~0.02 and less variable, and consequently DNI_{obs} is slightly larger.

Perspectives consist in validating SolaRes in more diverse conditions, as in arid environment strongly affected by desert dust, as already done for *DNI* with the ASoRA method [Elias *et al.*, 2021]. More studies are also necessary for computations in tilted planes, investigating on the influence of environment by reflection of the solar radiation. SolaRes may be improved by considering the spectral dependence of surface albedo, and even bidirectional reflectance distribution function, above all when dealing with solar resource assessment in tilted planes. To

complete the validation in all-sky conditions, the simulation of the cloud influence by SolaRes in global mode will be evaluated against ground-based measurements. Solar resource can also be evaluated in a complex physical environment embedded in a realistic changing atmosphere, even considering 3D interactions between solar radiation and the environment. Moulana *et al.* [2019] present preliminary work on the increased precision on solar resource assessment in a tower concentrated thermal solar plant using SMART-G, and Moulana *et al.* [Submitted] present the technology to adapt SMART-G to consider reflection with 3D objects.

References

Anderson, G., Clough, S., Kneizys, F., Chetwynd, J., and Shettle, E., Tech. Rep. AFGL-TR-86-0110, Air Force Geophys. Lab., Hanscom Air Force Base, Bedford, Mass, 1986.

Beck, H. E., Zimmermann, N. E., McVicar, T. R., Vergopolan, N., Berg, A., andWood, E. F.: Present and future Köppen-Geiger climate classification maps at 1-km resolution, Sci. Data, 5, 180214, https://doi.org/10.1038/sdata.2018.214, 2018.

Benedetti, A., Morcrette, J.-J., Boucher, O., Dethof, A., Engelen, R., Fisher, M., Flentje, H., Huneeus, N., Jones, L., Kaiser, J., Kinne, S., Mangold, A., Razinger, M., Simmons, A. J., and Suttie, M.: Aerosol analysis and forecast in the European centre for medium-range weather forecasts integrated forecast system: 2. Data assimilation, J. Geophys. Res.-Atmos., 114, D13205, https://doi.org/10.1029/2008JD011235, 2009.

Blanc, P., Espinar, B. , Geuder, N., Gueymard, C., Meyer, R., Pitz-Paal, R., Reinhardt, B., Renné, D., Sengupta, M., Wald, L., and Wilbert, S.: Direct normal irradiance related definitions and applications: The circumsolar issue, Solar Energy, 110, 561–577, 2014.

Bodhaine, B. A., Wood, N. B., Dutton, E. G., and Slusser, J. R.: On Rayleigh Optical Depth Calculations, J. Atm. Ocean Technol., 16, 1854–1861, https://doi.org/10.1175/1520-0426(1999)016%3C1854:ORODC%3E2.0.CO;2, 1999.

Bogumil, K., Orphal, J., Voigt, S., Spietz, P., Fleischmann, O. C., Vogel, A., Hartmann, M., Kromminga, H., Bovensmann, H., and Burrows, J. P.: Measurements of Molecular Absorption Spectra with the SCIAMACHY Pre-Flight Model: Instrument Characterization and Reference Data for Atmospheric Remote-Sensing in the 230-2380 nm Region, J. Photochem. and Photobio. A., 157, 167–184, 2003.

Chen, C., O. Dubovik,G.L. Schuster, D. Fuertes, Y. Meijer, J. Landgraf, Y. Karol, Z. Li, Characterization of temporal and spatial variability of aerosols from ground-based climatology: towards evaluation of satellite mission requirements, J.Q.S.R,T., 268, 2021, doi:10.1016/j.jqsrt.2021.107627

Driemel, A., Augustine, J., Behrens, K., Colle, S., Cox, C., Cuevas-Agulló, E., Denn, F. M., Duprat, T., Fukuda, M., Grobe, H., Haeffelin, M., Hodges, G., Hyett, N., Ijima, O., Kallis, A., Knap, W., Kustov, V., Long, C. N., Longenecker, D., Lupi, A., Maturilli, M., Mimouni, M., Ntsangwane, L., Ogihara, H., Olano, X., Olefs, M., Omori, M., Passamani, L., Pereira, E. B., Schmithüsen, H., Schumacher, S., Sieger, R., Tamlyn, J., Vogt, R., Vuilleumier, L., Xia, X., Ohmura, A., and König-Langlo, G.: Baseline Surface Radiation Network (BSRN): structure and data description (1992–2017), Earth Syst. Sci. Data, 10, 1491-1501, doi:10.5194/essd-10-1491-2018, 2018.

Dubovik, O., A. Smirnov, B. N. Holben, M. D. King, Y.J. Kaufman, T. F. Eck, and Slutsker, I.: Accuracy assessments of aerosol optical properties retrieved from AERONET sun and sky-radiance measurements, *J. Geophys. Res*., 105, 9791-9806, 2000.

Dubovik, O., B. Holben, T. Eck, A. Smirnov, Y. Kaufman, M. King, D. Tanré, and Slutsker, I.: Variability of absorption and optical properties of key aerosol types observed in worldwide locations, J. Atmos. Sci., 59, 590-608, 2002.

Dupont, J.-C. et al. (2016). « Role of the boundary layer dynamics effects on an extreme air pollution event in Paris». In : Atmospheric Environment 141, p. 571-579. ISSN : 1352-2310. DOI : https: //doi.org/10.1016/j.atmosenv.2016.06.061.

Elias, T., Ramon, D., Brau, J.-F., and Moulana, M.: Sensitivity of the solar resource in solar tower plants to aerosols and water vapor, AIP Conference Proceedings, 2126, 190006, 2019.

Elias, T., Ramon, D., Dubus, L., Am-Shallem, M., and Kroyzer, G.: DNI and slant path transmittance for the solar resource of tower thermal solar plants: The validation of the ASoRA method and impact in exploiting a global data set, Solar Energy, 217, 78-92, doi.org/10.1016/j.solener.2020.12.064, 2021.

Emde, C., R. Buras, B. Mayer, and Alis: An efficient method to compute high spectral resolution polarized solar radiances using the Monte Carlo approach, Journal of Quantitative Spectroscopy and Radiative Transfer, 112, 1622–1631, 2011.

Favez,O.;Weber,S.;Petit,J.-E.; Alleman, L.Y.; Albinet, A.;Riffault, V.; Chazeau, B.; Amodeo, T.; Salameh, D.; Zhang, Y.; et al.Overview of the French Operational Network for In Situ Observation ofPM Chemical Composition andSources in Urban Environments(CARA Program). Atmosphere 2021,12, 207. https://doi.org/10.3390/ atmos12020207.

Flowers, E. C., and Maxwell, E. L.: Characteristics of network measurements, Sol. Cells, 18, 205–212, 1986.

García, R. D., García, O. E., Cuevas, E., Cachorro, V. E., Romero-Campos, P. M., Ramos, R. and de Frutos, A. M.: Solar radiation measurements compared to simulations at the BSRN Izaña station. Mineral dust radiative forcing and efficiency study, Journal of Geophysical Research: Atmospheres, 119, 179-194, 2014.

Gelaro, R., McCarty, W., Suárez, M. J., Todling, R., A. Molod, L. Takacs, C. A. Randles, A. Darmenov, M. G. Bosilovich, Reichle, R., et al., The modern-era retrospective analysis for research and applications, version 2 (merra-2), Journal of Climate 30, 14, 5419–5454. doi:10.1175/JCLI-D-16-0758.1., 2017.

Giles, D. M., Sinyuk, A., Sorokin, M. G., Schafer, J. S., Smirnov, A., Slutsker, I., Eck, T. F., Holben, B. N., Lewis, J. R., Campbell, J. R., Welton, E. J., Korkin, S. V., and Lyapustin, A. I.: Advancements in the Aerosol Robotic Network (AERONET) Version 3 database – automated near-real-time quality control algorithm with improved cloud screening for Sun photometer aerosol optical depth (AOD) measurements, Atmos. Meas. Tech., 12, 169–209, https://doi.org/10.5194/amt-12-169-2019, 2019.

Gueymard, C. A.: Temporal variability in direct and global irradiance at various time scales as affected by aerosols, Solar Energy, 86, 12, 3544–3553. doi:10.1016/j.solener.2012.01.013, 2012.

Gueymard, C. A.: A review of validation methodologies and statistical performance indicators for modeled solar radiation data: Towards a better bankability of solar projects, Renewable and Sustainable Energy Reviews, 39, 1024-1034, doi.org/10.1016/j.rser.2014.07.117, 2014.

Gueymard, C. A., J. M. Bright, D. Lingfors, A. Habte, and M. Sengupta, M.; A posteriori clear-sky identification methods in solar irradiance time series: Review and preliminary validation using sky imagers, Renewable and Sustainable Energy Reviews, 109, 412-427, 2019.

Gueymard, C. A., and Ruiz-Arias, J.: Validation of direct normal irradiance predictions under arid conditions: A review of radiative models and their turbidity-dependent performance, Renewable and Sustainable Energy Reviews, 45, 379-396, 2015.

Gueymard, C. A. and Yang, D.: Worldwide validation of CAMS and MERRA-2 reanalysis aerosol optical depth products using 15 years of AERONET observations, Atmospheric Environment, 225, 117 216, https://doi.org/10.1016/j.atmosenv.2019.117216, 2020.

Gschwind, B., L. Wald, P. Blanc, M. Lefèvre, M. Schroedter-Homscheidt, et al., Improving the McClear model estimating the downwelling solar radiation at ground level in cloud-free conditions – McClear-v3, *Meteorologische Zeitschrift*, 28 (2) (2019), 147-163.

Hess, M., Koepke, P., Schult, I., 1998. Optical Properties of Aerosols and Clouds: The software package OPAC. Bull. Am. Met. Soc. 79, 831–844.

Holben, B., Eck, T., Slutsker, I., Tanré, D., Buis, J., Setzer, A., Vermote, E., Reagan, J., Kaufman, Y., Nakajima, T., Lavenu, F., Jankowiak, I., Smirnov, A., 1998. AERONET—A Federated Instrument Network and Data Archive for Aerosol Characterization, Remote Sensing of Environment. 66, 1 – 16.

Iacono, M. J., J. S. Delamere, E. J. Mlawer, M. W. Shephard, S. A. Clough, and W. D. Collins, Radiative forcing by long-lived greenhouse gases: Calculations with the AER radiative transfer models, J. Geophys. Res., 113 (2008) D13103. doi:10.1029/2008JD009944.

Kasten, F., A.T. Young. Revised optical air mass tables and approximation formula. Appl. Optics 28 (1989) 4735–4738.

Kato, S., T. P. Ackerman, Mather, J.H., E.E. Clothiaux, The k-distribution method and correlated-k approximation for a shortwave radiative transfer model, J. Quant. Spectrosc. Radiat. Transfer, 62 (1999) 109–121.

Kipp & Zonen (2008), Instruction Manual – CHP1 Pyrheliometer. [Available at http://www.kippzonen.com/Download/202/CHP1-Pyrheliometer-Manual, accessed 18/06/2014.]

Kipp & Zonen (2013), Instruction Manual – CMP series Pyranometer – CMA series Albedometer. [Available at http://www.kippzonen.com/Download/72/Manual-Pyranometer-CMP-series-English, accessed 18/06/2014.]er 62, 109–121.

Kurucz, R., 1992. Synthetic infrared spectra. In: Proceedings of the 154th Symposium of the International Astronomical Union (IAU); Tucson, Arizona, March 2–6, 1992, Kluwer, Acad., Norwell, MA.

Lacis, A.A., and V. Oinas, 1991: A description of the correlated k distributed method for modeling nongray gaseous absorption, thermal emission, and multiple scattering in vertically inhomogeneous atmospheres. *J. Geophys. Res.*, **96**, 9027-9063, doi:10.1029/90JD01945.

Lefèvre, M., A. Oumbe, P. Blanc, Espinar, B., Gschwind, B., Qu, Z., Wald, L., Schroedter-Homscheidt, M., Hoyer-Klick, C., Arola, A., Benedetti, A., Kaiser, J.W., J. J. Morcrette, McClear: a new model estimating downwelling solar radiation at ground level in clear-sky conditions. Atmos. Meas. Tech. 6 (2013), 2403–2418.

Lindsay, N., Q. Libois, J. Badosa, A. Migan-Dubois, V. Bourdin, Errors in PV power modelling due to the lack of spectral and angular details of solar irradiance inputs, Solar Energy, 197 (2020) 266-278. https://doi.org/10.1016/j.solener.2019.12.042.

Long, C. N. and T. P. Ackerman, Identification of clear skies from broadband pyranometer measurements and calculation of downwelling shortwave cloud effects, Journal of Geophysical Research: Atmospheres, 105 (2000) 15609-15626.

Marchuk, G., G. Mikhailov, M. Nazaraliev, R. Dacbinjan, B. Kargin, B. Elepov, Monte carlo methods in atmospheric optics, Applied Optics 20 (1981).

Mercado, L., Bellouin, N., Sitch, S. *et al.* Impact of changes in diffuse radiation on the global land carbon sink. *Nature* **458**, 1014–1017 (2009). https://doi.org/10.1038/nature07949 .

Michalsky, J. J., L. Harrison, Cosine response characteristics of some radiometric and photometric sensors, Solar Energy, June 1995, doi:10.1016/0038-092X(95)00017-L

Michalsky, J. J., E. Dutton, M. Rubes, D. Nelson, T. Stoffel, M. Wesley, M. Splitt, and J. DeLuisi, Optimal measurement of surface shortwave irradiance using current instrumentation, J. Atmos.

Ocean. Technol, 16 (1999) 55–69. doi:10.1175/1520-0426(1999)016%3C0055:OMOSSI%3E2.0.CO;2.

Michalsky, J. J., G. Anderson, J. Barnard, J. Delamere, C. Gueymard, S. Kato, P. Kiedron, A. McComiskey, and P. Ricchiazzi, Shortwave radiative closure studies for clear skies during the Atmospheric Radiation Measurement 2003 Aerosol Intensive Observation Period, J. Geophys. Res., 111 (2006), D14S90. doi:10.1029/2005JD006341.

Mol, W., B. Heusinkveld, M.R. Mangan, O. Hartogensis, M. Veerman, C. van Heerwaarden, Observed patterns of surface solar irradiance under cloudy and clear-sky conditions, Q.J.R.M.S., March 2024, doi : 10.1002/qj.4712

Morcrette, J.-J., O. Boucher, L. Jones, Salmond, D., Bechtold, P., Beljaars, A., Benedetti, A., Bonet, A., Kaiser, J., Razinger, M., Schulz, M., Serrar, S., Simmons, A. J., Sofiev, M., Suttie, M., Tompkins, A. M., and Untch, A.: Aerosol analysis and forecast in the European Centre for medium-range weather forecasts integrated forecast system: Forward modeling, J. Geophys. Res. Atmos., 114 (2009) D06206. https://doi.org/10.1029/2008JD011235.

Moulana, M., Elias, T., C. Cornet, D. Ramon, First results to evaluate losses and gains in solar radiation collected by Solar Tower Plants, AIP Conference Proceedings, 2126 (2019) 190012.

Moulana, M., C. Cornet, T. Elias, D. Ramon, C. Caliot, M. Compiègne, Concentrated solar flux modeling in solar power towers with a 3D objects-atmosphere hybrid system, Solar Energy, Submitted.

Mubarak, R.; Hofmann, M.; Riechelmann, S.; Seckmeyer, G. Comparison of Modelled and Measured Tilted Solar Irradiance for Photovoltaic Applications. *Energies* **2017**, *10*, 1688. https://doi.org/10.3390/en10111688

Ningombam, S. S., E. Larson, Dumka, U.; Estellés, V.; Campanelli, M. and C. Steve, Long-term (1995–2018) aerosol optical depth derived using ground based AERONET and SKYNET measurements from aerosol aged-background sites, Atmospheric Pollution Research, 10 (2019) 608-620.

Ohmura, A., H. Gilgen, H. Hegner, G. Mueller, M. Wild, E.G. Dutton, B. Forgan, C. Froelich, R. Philipona, A. Heimo, G. Koenig-Langlo, B. McArthur, R. Pinker, C.H. Whitlock, K. Dehne, Baseline Surface Radiation Network (BSRN/WCRP): New precision radiometry for climate research, Bull. Amer. Meteor. Soc. 79, (1998) 2115–2136. DOI: 10.1175/1520-0477.

Papayannis, A., et al. (2008), Systematic lidar observations of Saharan dust over Europe in the frame of EARLINET (2000–2002), *J. Geophys. Res.*, 113, D10204, doi:10.1029/2007JD009028.

Perez, R., P. Ineichen, R. Seals, J. Michalsky, R. Stewart, Modeling daylight availability and irradiance components from direct and global irradiance, Solar Energy. 44 (1990), 271-289.

Qu, Z., A. Oumbe, P. Blanc, B. Espinar, G. Gesell, et al., Fast radiative transfer parameterisation for assessing the surface solar irradiance: The Heliosat-4 method, Meteorologische Zeitschrift. 26 (1) (2017), 33-57.

Ramon, D., F. Steinmetz, D. Jolivet, M. Compiègne, R. Frouin, Modeling polarized radiative transfer in the ocean-atmosphere system with the gpu-accelerated smart-g monte carlo code, Journal of Quantitative Spectroscopy and Radiative Transfer. 222-223 (2019), 89–107. https://doi.org/10.1016/j.jqsrt.2018.10.017

Ruiz-Arias J. A., J. Dudhia, F. J. Santos-Alamillos, and Pozo-Vázquez, D.: Surface clear-sky shortwave radiative closure intercomparisons in the Weather Research and Forecasting model, J Geophys Res., 118, 9901–9913. https://doi.org/10.1002/jgrd.50778, 2013.

Salamalikis, V., I. Vamvakas, P. Blanc, A. Kazantzidis, Ground-based validation of aerosol optical depth from CAMS reanalysis project: An uncertainty input on direct normal irradiance under cloud-free conditions, Renewable Energy, 170, 2021, 847-857, https://doi.org/10.1016/j.renene.2021.02.025.

Sinyuk, A., B. N. Holben, T. F. Eck, D. M. Giles, I. Slutsker, S. Korkin, J. S. Schafer, A. Smirnov, M. Sorokin, and Lyapustin, A.: The AERONET Version 3 aerosol retrieval algorithm, associated uncertainties and comparisons to Version 2, Atmos. Meas. Tech., 13, 3375–3411. https://doi.org/10.5194/amt-13-3375-2020, 2020.

Sun, X., J. M. Bright, C. A. Gueymard, B. Acord, P. Wang, and Engerer, N. A.: Worldwide performance assessment of 75 global clear-sky irradiance models using Principal Component Analysis, Renewable and Sustainable Energy Reviews, 111, 550-570, https://doi.org/10.1016/j.rser.2019.04.006, 2019.

Witthuhn, J., Hünerbein, A., Filipitsch, F., Wacker, S., Meilinger, S., and Deneke, H.: Aerosol properties and aerosol–radiation interactions in clear-sky conditions over Germany, Atmos. Chem. Phys. 21, 14591–14630, https://doi.org/10.5194/acp-21-14591-2021, 2021.

Acknowledgements: LOA staff is acknowledged for providing the observation data set of Lille composed by GHI, DNI, DifHI and GTI, as well as BSRN for the observation data set of Palaiseau made of GHI, DNI and DifHI. AERONET is also acknowledged for the data set of AOT, WVC and inverted aerosol model products, as well as Philippe Goloub as PI of the Lille and Palaiseau stations. And CAMS is also acknowledged for providing the AOT data.

Competing interests: The contact author has declared that none of the authors has any competing interests.

Author contribution: GC wrote the Section 4 and developed the cloud-screening codes. TE and MM developed the SolaRes code and TE made the SolaRes computations for the paper. TE wrote the other Sections of the manuscript. NF is the Lille instrument PI. NF and IC are the Ph. D. supervisors of GC. All authors contributed on discussions about the work in progress, and all authors made comments on the paper writing.